nature communications

Article

https://doi.org/10.1038/s41467-025-59298-w

Two-stage CD8$^+$ CAR T-cell differentiation in patients with large B-cell lymphoma

Received: 6 December 2024

Accepted: 16 April 2025

Published online: 06 May 2025

Check for updates

Guoshuai Cao[1,8], Yifei Hu[2,8], Tony Pan[1,8], Erting Tang[1], Nicholas Asby[1], Thomas Althaus[3], Jun Wan[4], Peter A. Riedell[3,5,6], Michael R. Bishop[3,5], Justin P. Kline[3,5,6,7] & Jun Huang[1,6,7]

Advancements in chimeric antigen receptor (CAR) T-cell therapy for treating diffuse large B-cell lymphoma (DLBCL) have been limited by an incomplete understanding of CAR T-cell differentiation in patients. Here, we show via single-cell, multi-modal, and longitudinal analyses, that CD8$^+$ CAR T cells from DLBCL patients successfully treated with axicabtagene ciloleucel undergo two distinct waves of clonal expansion in vivo. The first wave is dominated by an exhausted-like effector memory phenotype during peak expansion (day 8–14). The second wave is dominated by a terminal effector phenotype during the post-peak persistence period (day 21–28). Importantly, the two waves have distinct ontogeny from the infusion product and are biologically uncoupled. Precursors of the first wave exhibit more effector-like signatures, whereas precursors of the second wave exhibit more stem-like signatures. We demonstrate that CAR T-cell expansion and persistence are mediated by clonally, phenotypically, and ontogenically distinct CAR T-cell populations that serve complementary clinical purposes.

Diffuse large B-cell lymphoma (DLBCL), the most common non-Hodgkin's lymphoma in the United States, is characterized by diffusely proliferating and malignant B cells at nodal or extranodal sites[1]. Although up-front chemoimmunotherapy is often curative, patients with DLBCL that is refractory to up-front treatment or relapse following remission (r/r DLBCL) have limited treatment options and poor outcomes[2,3]. Effective treatment options were limited until the United States Food and Drug Administration approved autologous CD19-directed chimeric antigen receptor (CAR) T-cell therapies for r/r DLBCL in 2017. Autologous CD19-directed CAR T-cell therapy involves virally transducing a patient's T cells ex vivo with a CD19-directed CAR —an engineered receptor consisting of an extracellular anti-CD19 single-chain variable fragment, a hinge/transmembrane region, and intracellular costimulatory (CD28 or 4-1BB) and activation (CD3ζ) domains. CAR-transduced T cells (i.e., CAR T cells) are cultured and infused into the patient, where they lyse CD19$^+$ lymphoma cells[4]. CD19-directed CAR T-cell therapy has achieved complete response rates of 40–54%[5–8] for r/r DLBCL, but non-response rates[6,9] and treatment toxicities[10] remain as challenges[11].

Development of CAR T-cell formulations with higher response rates and fewer toxicities requires a thorough understanding of how CAR T cells differentiate in patients with r/r DLBCL. The pioneering ZUMA-1 trial (NCT02348216) for axicabtagene ciloleucel (autologous CD28-costimulated CAR T cells) demonstrated that peripheral blood CAR T cells expand, contract, and sometimes persist.[5] Greater expansion predicted higher response rates, but also higher likelihood of developing treatment toxicities[5,12]. Longer persistence predicted durable remission and long-term immunosurveillance with leukemias, but its relevance for preventing DLBCL relapse remains obscure[9,13]. Although many factors are associated with expansion and persistence

[1]Pritzker School of Molecular Engineering, University of Chicago, Chicago, IL 60637, USA. [2]Pritzker School of Medicine, University of Chicago, Chicago, IL 60637, USA. [3]The David and Etta Jonas Center for Cellular Therapy, University of Chicago, Chicago, IL 60637, USA. [4]Department of Medical and Molecular Genetics, Indiana University School of Medicine, Indianapolis, IN 46202, USA. [5]Department of Medicine, University of Chicago, Chicago, IL 60637, USA. [6]Committee on Cancer Biology, University of Chicago, Chicago, IL 60637, USA. [7]Committee on Immunology, University of Chicago, Chicago, IL 60637, USA. [8]These authors contributed equally: Guoshuai Cao, Yifei Hu, Tony Pan. e-mail: huangjun@uchicago.edu

(including CAR design[14,15] and CAR T-cell phenotypes[16–20], among others[21–23]), how and why CAR T cells differentiate into expansive or persistent phenotypes in vivo is still an open question. Addressing this question requires a single-cell approach that integrates CAR T-cell phenotypes and clonal kinetics over longitudinal timepoints. However, existing studies have either focused on CAR T-cell phenotypes[19,24,25] or clonal kinetics[26] without integrating both data modalities, or lacked the temporal resolution required to decipher cell fates over longer periods[12,27]. Consequently, a complete and longitudinal understanding of CAR T-cell differentiation in vivo has remained elusive.

To comprehensively elucidate CAR T-cell differentiation in vivo, we perform single-cell, multi-modal (paired RNA-seq/CITE-seq/TCR-seq), and longitudinal analyses of CD28-costimulated CAR T cells from infusion product and peripheral blood of seven patients with r/r DLBCL who were complete responders under treatment with axicabtagene ciloleucel. Peripheral blood CAR T cells are sorted using CD19 antigen-tetramers[28]. Importantly, we report that the CD8$^+$ CAR T cells observed during the peak expansion period (day 8–14) have distinct clonotypic repertoires compared to the later CD8$^+$ CAR T cells observed during the post-peak persistence period (day 21–28). We further analyze how these two CAR T-cell populations differ with respect to phenotypes, transcriptional profiles, regulatory networks, and infusion product precursors. Our findings not only offer a finer understanding of CAR T-cell biology in vivo, but also inform efforts to develop CAR T cells with improved expansion and persistence.

Results

Study design and clinical findings

To interrogate CD28-costimulated CAR T-cell differentiation in vivo, we longitudinally interrogated the phenotypes and clonal dynamics of CAR T cells from seven patients (P1-7) who achieved complete responses under treatment with axicabtagene ciloleucel (Fig. 1a). Patients were diagnosed with r/r DLBCL and treated at the University of Chicago Medicine between 2019 and 2021 (Table 1). Clinical response

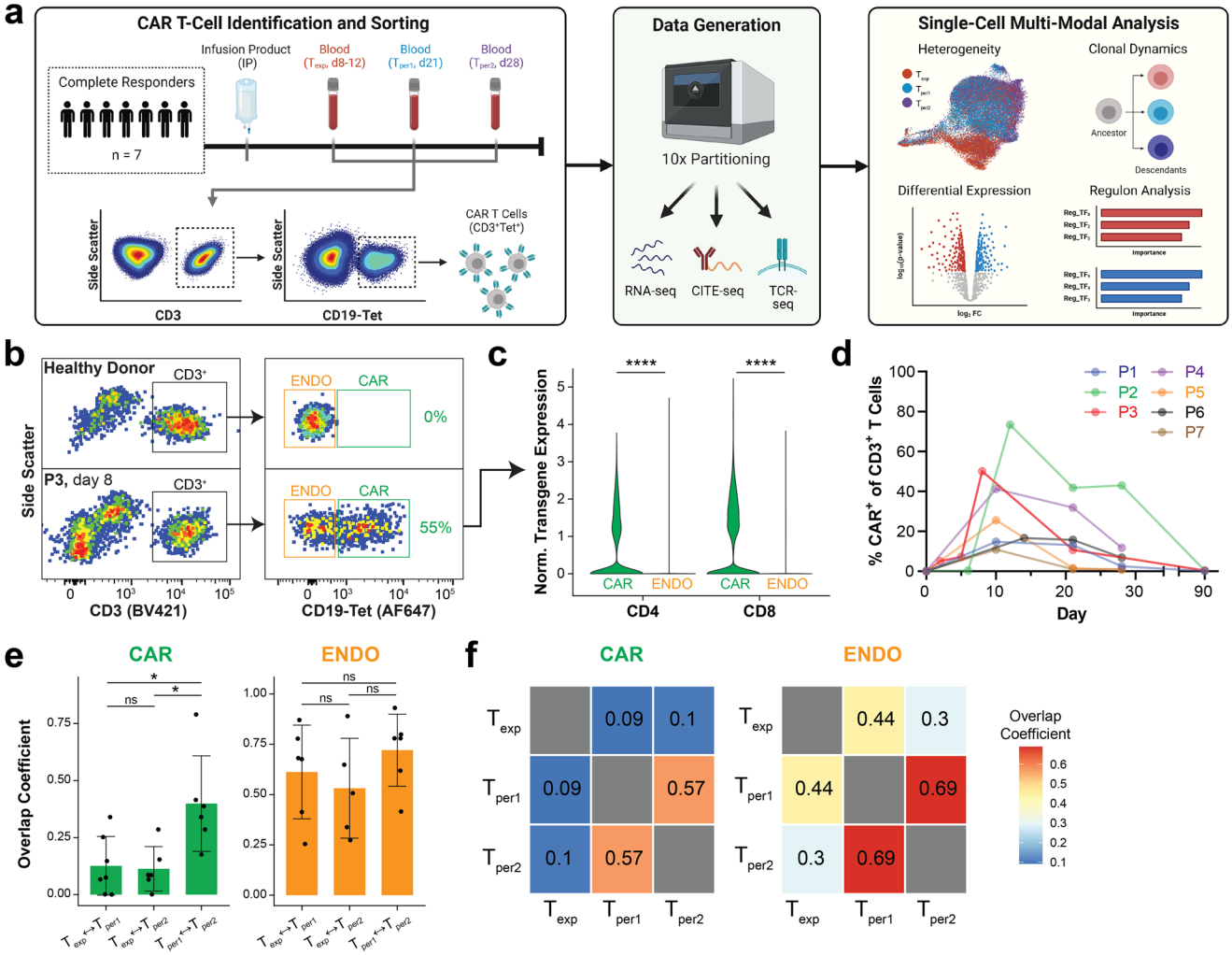

Fig. 1 | CD8$^+$ CAR T cells from complete responders undergo a clonotypic shift in vivo. a Schematic depicting sorting strategy, data generation, and single-cell multi-modal analysis of CAR T cells in peripheral blood from seven CAR T-cell therapy patients (P1-7) who exhibited complete responses with axicabtagene ciloleucel. Created in BioRender. Hu, Y. (2025) https://BioRender.com/hqo12oz. **b** Representative flow plots depicting anti-CD3 and CD19 antigen-tetramer staining of peripheral blood mononuclear cells from P3 versus a healthy donor. CD3$^+$Tet$^+$ ("CAR") and CD3$^+$Tet$^-$ ("ENDO") patient cells were sorted from the indicated gates. **c** Violin plots depicting normalized CAR transgene mRNA expression of sorted CAR and ENDO T cells, split by CD4$^+$ (left) and CD8$^+$ (right) subsets. Expression levels were compared by two-sided Wilcoxon Rank-Sum test with Bonferroni correction, whereby **** indicates $p < 0.0001$. **d** Line plots depicting expansion and contraction of peripheral blood CAR abundance over the course of therapy. **e**, **f** Bar graphs and heatmaps depicting overlap coefficients for TCR clonotypes comparing CAR (left) and ENDO (right) repertoires between T_{exp}, T_{per1}, and T_{per2}. Overlap coefficients were compared by two-sided t test, whereby * indicates $p < 0.05$ and ns indicates not significant. Each dot represents a measurement from a single patient ($n = 7$). Data are presented as mean values ± SEM. Exp expansion stage, Per persistence stage. Source data are provided as a Source Data file.

Table 1 | Patient characteristics and relevant clinical data

Characteristics	P1	P2	P3	P4	P5	P6	P7
Age Decade	70s	60s	50s	50s	40s	60s	60s
Sex	Male	Male	Female	Female	Male	Male	Female
Disease stage	II	IV	II	I	IV	IV	IV
No. of prior therapies	2	5	2	4	5	3	3
Prior lines of therapy	R-CHOP	R-CHOP	DA-EPOCH w/ IT MTX	Radiation	R-CHOP	R-CHOP	R-CHOP
	R-ICE	Benda-obinutuzumab	ICE	R-CHOP	R-ICE	R-ICE	R-ICE
		R-ICE		R-ICE	BEAM + ASCT	BEAM + ASCT	BEAM + ASCT
		Hu5F9-G4 + rituximab		BEAM + ASCT	FCR + AlloSCT		
		R-GEMOX			R-GEMOX		
Disease status	Relapsed	Relapsed, then refractory	Primary refractory	Relapsed	Relapsed	Relapsed	Relapsed
Baseline (Ref. range)							
LDH, U/L (116-245 U/L)	165	311	312	186	203	1276	297
CRP, mg/dL (< 0.5 mg/dL)	0	ND	3.5	0.6	0.3	4.1	1.4
Ferritin, ng/mL (20-300 ng/mL)	110	ND	576	215	544	1228	229
ECOG PS	1	1	2	0	1	1	0
Bridging therapy	No	No	Yes	No	Yes	Yes	No
Maximum Grade CRS	2	1	2	1	1	1	1
Maximum Grade ICANS	2	3	3	4	1	1	0
Tocilizumab or steroids	Both	Both	Both	Steroids	Tocilizumab	Tocilizumab	Tocilizumab
Survival status	Deceased	Alive	Deceased	Alive	Alive	Alive	Alive
Cause of Death	Second Malignancy	---	Progressive lymphoma	---	---	---	---

ASCT autologous stem cell transplant, *AlloSCT* allogeneic stem cell transplant, *BEAM* BCNU (carmustine), etoposide, cytarabine, melphalan, *CRP* C-reactive protein, *CRS* cytokine release syndrome, *DA-EPOCH* dose-adjusted etoposide, prednisone, oncovin, cyclophosphamide, hydroxydaunorubicin, *ECOG PS* Eastern Cooperative Oncology Group Performance Score, *FCR* fludarabine, cyclophosphamide, rituximab, *Hu5F9-G4* magrolimab, *ICANS* immune effector cell-associated neurotoxicity syndrome, *ICE* ifosfamide, carboplatin, etoposide, *IT MTX* intrathecal methotrexate, *LDH* lactate dehydrogenase, *ND* not determined, *R-CHOP* rituximab, cyclophosphamide, hydroxydaunorubicin, oncovin, prednisone, *R-GEMOX* rituximab, gemcitabine, oxaliplatin, *R-ICE* rituximab, ifosfamide, carboplatin, etoposide.

was determined by positron emission tomography/computed tomography imaging 30 days after infusion product administration. Complete response was defined as no detectable lymphoma (Fig. S1). To capture phenotypic heterogeneity and clonal dynamics longitudinally, we performed single-cell multi-modal analyses (paired RNA-seq/CITE-seq/TCR-seq via the 10x Genomics platform) on infusion product and peripheral blood biospecimens at three timepoints: peak expansion (T_{exp}, day 8–14), early post-peak persistence (T_{per1}, day 21), and late post-peak persistence (T_{per2}, day 28) (Table 2). The three peripheral blood timepoints were available for all patients, except P3 (only T_{exp} and T_{per1}). CAR T cells were sorted from peripheral blood using CD19 antigen-tetramers (representative staining in Fig. 1b, Fig. S2)[28]. Compared to CD19 antigen-tetramer-negative T cells, CD19 antigen-tetramer-positive T cells specifically expressed the CAR transgene, which validates our sorting strategy (Fig. 1c).

$CD8^+$ CAR T cells undergo a clonotypic shift between T_{exp} and T_{per}

To analyze CAR T-cell population dynamics, we tracked CAR abundance (% CAR^+ of $CD3^+$ T cells) in peripheral blood throughout the course of therapy. CAR abundance at peak expansion ranged from 11% to 73% (Fig. 1d). Peak expansion occurred at day 8–14, which is consistent with prior clinical findings[5]. For each timepoint, we quantified proportions of $CD8^+$ and $CD4^+$ T cells within the total CAR T-cell population by single-cell RNA-seq and CITE-seq. CAR T cells were predominantly $CD8^+$ across most patients and timepoints (Fig. S3).

We next analyzed the dynamics of the CAR T-cell clonal repertoire across longitudinal timepoints (T_{exp} at day 8–14, T_{per1} at day 21, T_{per2} at day 28) using single-cell TCR-seq. Clone sizes were similar across timepoints (Fig. S4a). Clonotypes did not overlap between patients (Fig. S4b). Repertoire overlap analysis indicated that T_{exp} clonotypes were significantly distinct from T_{per1} or T_{per2} clonotypes (Fig. 1e, f, left). In sharp contrast, T_{per1} and T_{per2} clonotypes overlapped substantially more. As a control, we also analyzed endogenous (non-CAR) T cells from matched timepoints. Unlike with CAR T cells, endogenous T cells did not show distinctive clonotypic patterns (Fig. 1e, f, right), indicating that the shift in clonotypes between T_{exp} and T_{per} is CAR-specific. This CAR-specific clonotypic shift was consistent across patients (Fig. S4b). Moreover, the distinction between T_{exp} and T_{per} clonotypes is driven by $CD8^+$ T cells, and not by $CD4^+$ T cells (Fig. S4c). Collectively, these findings indicate that $CD8^+$ CAR T cells undergo a clonotypic shift between T_{exp} and T_{per}.

$CD8^+$ CAR T cells undergo a phenotypic shift from exhausted-like effector memory to terminal effector

Having shown a shift in $CD8^+$ CAR T-cell clonotypes between T_{exp} and T_{per}, we hypothesized that unique $CD8^+$ CAR T-cell phenotypes dominate T_{exp} and T_{per}. To test this hypothesis, we filtered $CD8^+$ CAR T cells for Uniform Manifold Approximation and Projection (UMAP) and identified six T-cell clusters (Fig. 2a) based on gene and protein markers (Fig. 2b, expanded marker set in Fig. S5a). No cluster was patient-specific (Fig. S5b). All clusters expressed CAR transgene and CD8α, validating our sorting and filtering processes, respectively. All clusters expressed *CXCR3*, a chemokine receptor that demarks activated T cells.

Examination of gene and protein markers revealed that one of the six clusters represented proliferating T cells (*MKI67*$^+$*TOP2A*$^+$). The remaining five non-proliferating clusters were annotated as central

Table 2 | Number of sequenced CD4⁺ and CD8⁺ CAR T cells for each sample

Patient	Timepoint	# of CD4⁺ CAR T cells	# of CD8⁺ CAR T cells
P1	IP	1021	2375
P1	T_{exp}	13	7
P1	T_{per1}	431	3347
P1	T_{per2}	166	1009
P2	IP	1734	1716
P2	T_{exp}	789	3383
P2	T_{per1}	542	2227
P2	T_{per2}	567	5370
P3	IP	754	3468
P3	T_{exp}	51	172
P3	T_{per1}	331	1597
P4	IP	1214	1081
P4	T_{exp}	1299	977
P4	T_{per1}	695	3633
P4	T_{per2}	224	1144
P5	IP	284	3656
P5	T_{exp}	205	1030
P5	T_{per1}	878	958
P5	T_{per2}	395	431
P6	T_{exp}	17	1041
P6	T_{per1}	126	4602
P6	T_{per2}	144	3805
P7	IP	1810	1360
P7	T_{exp}	1402	3043
P7	T_{per1}	53	80
P7	T_{per2}	100	169

memory (CM, *TCF7*⁺*TBX21*⁻), effector memory (EM, *TCF7*⁺*TBX21*⁺), or terminal effector (TE, *TCF7*⁻*TBX21*⁺) T cells. The *TCF7*⁺*TBX21*⁻ CM cluster exhibited markers of stemness (*IL7R*, high CD127) and minimal markers of effectorness (*GZMB*, *CX3CR1*). The two *TCF7*⁺*TBX21*⁺ EM clusters occupied the lower half of the UMAP and uniquely expressed *CXCR6*, a chemokine receptor that facilitates trafficking into solid tumors[29]. One of these EM clusters upregulated markers consistent with early exhaustion (*NR4A2*, *TOX*, *GZMK*, low TIM-3), hence it was designated "exhausted-like EM". Lastly, the two *TCF7*⁻*TBX21*⁺ TE clusters occupied the upper half of the UMAP and uniquely downregulated *GZMK*. One of these TE clusters upregulated markers consistent with late exhaustion (*TOX*, *PDCD1*, high TIM-3), hence it was designated "exhausted-like TE". The other TE cluster was highly clonal (some clone sizes >100), suggesting expansion through proliferation (Fig. S7a). Overall, most CD8⁺ CAR T cells were *TBX21*⁺ EM or TE, which is consistent with the established link between CD28 costimulation and effector memory (rather than central memory) differentiation[14,15].

Phenotypic compositions of CD8⁺ CAR T cells at T_{exp} and T_{per} were compared. CAR T cells at T_{exp} were predominantly exhausted-like EM (64%) whereas CAR T cells at T_{per} were predominantly TE (63% for T_{per1}, 77% for T_{per2}) (Fig. 2c). These findings were statistically significant and consistent across all seven patients (Fig. 2d, Fig. S5c). Moreover, the large clone sizes within the T_{per}-specific TE cluster (Fig. S7a) suggest active TE proliferation at T_{per}. CAR T cells at T_{per1} were enriched for EM. From T_{per1} to T_{per2}, the EM proportion decreased while the TE proportion increased, suggesting progressive differentiation from EM to TE. However, the overall phenotypic compositions at T_{per1} and T_{per2} were more similar than different, which is concordant with findings from repertoire overlap analysis (Fig. 1e, f). Moreover, we observed decreasing proliferating proportions and increasing CM proportions over time (Fig. 2d), though this was not always statistically significant. These changing proportions may suggest some CAR T cells were returning from an activated to a resting phenotype. In conclusion, CD8⁺ CAR T cells phenotypically shifted from exhausted-like EM to TE between T_{exp} and T_{per}.

CD4⁺ CAR T cells maintain a memory phenotype with CAR Treg persistence

We next performed clustering, annotation, and longitudinal analyses of CD4⁺ CAR T cells to investigate phenotypes at T_{exp} and T_{per}. We identified five T-cell clusters, all expressing CAR transgene and CD4, based on gene and protein markers (Fig. 2e, f; expanded marker set in Fig. S6a). No cluster was patient-specific (Fig. S6b). All clusters expressed *CXCR3*, indicating T-cell activation and type 1 helper polarization.

One of the five clusters represented proliferating T cells (*MKI67*⁺*TOP2A*⁺). The remaining four non-proliferative clusters were annotated as memory (Mem, *TBX21*⁻*FOXP3*⁻), type 1 helper (Th1, *TBX21*⁺*FOXP3*⁻), or regulatory (Treg, *TBX21*⁻*FOXP3*⁺) T cells. The two *TBX21*⁻*FOXP3*⁻ Mem clusters at the center of the UMAP comprised most of the cells. One of the Mem clusters upregulated *IRF7* and interferon-stimulated genes (*MX1*, *OAS1*, *ISG15*), indicating response to type I interferon signaling. This signature suggests dynamic interferon secretion in vivo and is in concordance with type I interferon's role in memory CD4⁺ T-cell differentiation[30]. The *TBX21*⁺*FOXP3*⁻ Th1 cluster along the lower half of the UMAP upregulated cytolytic genes (*PRF1*, *GNLY*, *GZMK*, *NKG7*) and tissue-homing chemokine receptors (*CX3CR1*, *CXCR6*), resembling the cytotoxic CD4⁺ CAR T cells described by Melenhorst et al.[19]. Lastly, the *TBX21*⁻*FOXP3*⁺ Treg cluster expressed classic Treg markers (*IL2RA*, CD25, low *IL7R*, low CD127) and upregulated *IKZF2*, indicating a suppressive phenotype[31]. CAR Tregs inhibit conventional CAR T cells[27,32] and portend progressive disease[12,27].

Phenotypic compositions of CD4⁺ CAR T cells at T_{exp} and T_{per} were compared. CD4⁺ CAR T cells predominantly exhibited a Mem phenotype (49–82%) across all timepoints (Fig. 2g). This observation was consistent across all patients (Fig. S6c). Between T_{exp} and T_{per1}, the Mem proportion significantly decreased while the Th1 proportion significantly increased, indicating that CD4⁺ CAR T cells may be increasingly polarized during the early contraction period (Fig. 2h). Moreover, across all patients, the Treg proportion steadily increased from T_{exp} (5%) to T_{per1} (11%) to T_{per2} (21%), indicating that CAR Tregs were maintained in peripheral blood after peak expansion. The CAR Treg cluster was predominantly non-clonal (Fig. S7b), suggesting CAR Tregs were maintained through persistence rather than proliferation. While previous studies have only investigated CAR Tregs at day 7[12,27], this current study affirms and extends the presence of CAR Tregs until at least day 28. Importantly, persistence of CAR Tregs points towards their possible involvement in decreasing acute inflammation and restoring immune homeostasis after peak expansion. In conclusion, we discovered that CD4⁺ CAR T cells did not exhibit an abrupt T_{exp}-to-T_{per} phenotypic shift. Rather, they consistently exhibited a memory phenotype with CAR Tregs persisting over the course of therapy.

Integration of clonotypic and phenotypic shifts in CD8⁺ CAR T cells supports a two-stage differentiation model

Having observed shifts in both CD8⁺ CAR T-cell clonotypes and phenotypes between T_{exp} and T_{per}, we hypothesized the existence of two distinct waves of in vivo clonal expansion. To test this hypothesis, we linked the clonotype and phenotype of single CD8⁺ CAR T cells in our dataset using their cell barcodes as unique indices. After this linking process, we confirmed that the proportions of T cells with exhausted-like EM (EM-exh) and terminal effector (TE) phenotypes (Fig. 3a) are consistent with prior results (Fig. 2c). A phenotype label was subsequently assigned to each CD8⁺ CAR T-cell clone based on its predominant phenotype at each timepoint. For each patient, we tracked

https://doi.org/10.1038/s41467-025-59298-w

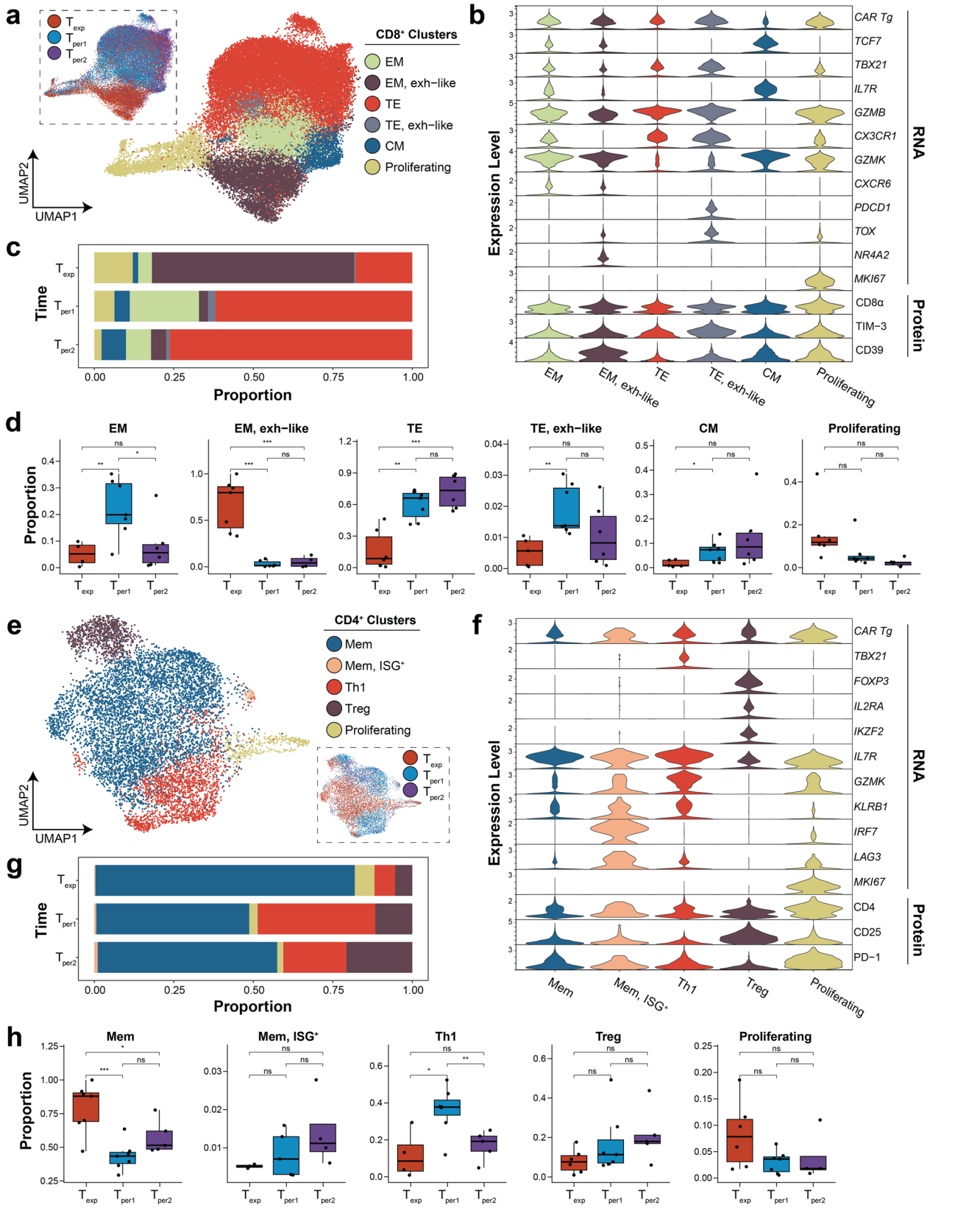

the total abundances of clones sharing a common phenotype label across timepoints. Notably, the abundance of EM-exh clones at T_{exp} was significantly reduced at T_{per1} and T_{per2} (Fig. 3b, left), while the abundance of TE clones at T_{per1} and T_{per2} was significantly reduced at T_{exp} (Fig. 3b, middle and right). In addition to redemonstrating the shifts in CD8⁺ CAR T-cell clonotypes and phenotypes, these findings support the existence of two distinct waves of in vivo clonal expansion. (Fig. 3c).

Next, we evaluated the explanatory power of our hypothesis for two distinct clonal waves. To minimize noise, we filtered for the top 500 largest clones (mean size 10.8, minimum size 4). Resulting clones were annotated with the following three definitions, based on our

Fig. 2 | Phenotypic heterogeneity of peripheral blood CD8⁺ and CD4⁺ CAR T cells. UMAPs depicting single-cell transcriptomes of CD8⁺ (**a**) and CD4⁺ (**e**) CAR T cells colored by cell cluster. Inset depicts distribution of transcriptomes across timepoints. Violin plots depicting normalized expression levels of key genes and proteins for annotating and phenotyping CD8⁺ (**b**) and CD4⁺ (**f**) CAR T cells. For extended versions, see Fig. S5a and S6a. Stacked bar graphs depicting proportions of each CD8⁺ (**c**) and CD4⁺ (**g**) CAR T-cell phenotype at different timepoints. Box-plots depicting proportion of CD8⁺ (**d**) and CD4⁺ (**h**) CAR T cells of a given phenotype at different timepoints. Each dot represents a measurement from a single patient ($n = 7$). The central line indicates the median. The bounds of the box indicate the 25th–75th percentile. The length of the whiskers indicates 1.5 times the inter-quartile range from the first and third quartiles. Proportions are compared between timepoints by two-sided t test, whereby *** indicates $p < 0.001$, ** indicates $p < 0.01$, * indicates $p < 0.05$, and ns indicates not significant. CM central memory, EM effector memory, TE terminal effector, Mem memory, ISG interferon stimulated genes, Th1 type 1 helper-like. Source data are provided as a Source Data file.

hypothesis for two waves: "Wave 1" (phenotypically EM-exh with highest abundance at T_{exp}), "Wave 2" (phenotypically TE with highest abundance at T_{per1}/T_{per2}), or "Other" (not Wave 1 or Wave 2). Wave 1 and Wave 2 clones together accounted for a significant majority (76%) of the top 500 clones (Fig. 3d). In accordance with our definitions, Wave 1 clones were maximally abundant at T_{exp}, while Wave 2 clones were maximally abundant at T_{per} (Fig. 3e). Wave 1 clones predominantly exhibited an EM-exh phenotype at T_{exp} and sharply decreased in abundance at T_{per} (Fig. 3f, left). In contrast, Wave 2 clones predominantly exhibited a TE phenotype at T_{per} and sharply decreased in abundance at T_{exp} (Fig. 3f, right). To investigate whether these findings are dependent on clone size, we expanded our analysis to the top 3000 largest clones (mean size 3.7, minimum size 2). Under this filter, Wave 1 and Wave 2 clones together continued to account for a significant majority (79%) of the top 3000 clones (Fig. S8a) and reaffirm the expected clonal and phenotypic dynamics (Fig. S8b, c). Therefore, our hypothesis for two distinct waves of in vivo clonal expansion has high explanatory power and is robust to clone size.

In conclusion, the two distinct waves of in vivo clonal expansion strongly substantiate a two-stage CD8⁺ CAR T-cell differentiation model (Fig. 3g). Under this model, some CAR T cells (Wave 1) with an exhausted-like EM phenotype expand earlier to dominate the peak expansion timeframe (T_{exp}), while other CAR T cells (Wave 2) with a TE phenotype expand later to dominate the post-peak persistence timeframe (T_{per}). Of note, the two-stage differentiation model uncouples CD8⁺ CAR T cells from peak expansion and post-peak persistence by designating these two waves as separate lineages. Moreover, these findings provide evidence against the intuitive idea that the post-peak contraction in CAR abundance is solely apoptosis or extravasation of short-lived CAR T cells from peak expansion. Rather, even as total CAR abundance contracts after peak expansion, a distinct subset of CAR T-cell clones simultaneously expands to eventually dominate the peripheral blood CAR T-cell repertoire.

T_{exp}- and T_{per}-specific transcriptional signatures and regulatory networks

We set out to identify the molecular determinants underlying CD8⁺ CAR T cells at T_{exp} and T_{per} using gene set enrichment analysis (GSEA), differential gene expression analysis (DGEA), and regulatory network analysis. For internal validation, the average expression of timepoint-specific genes (see Methods) for each sample (patient by timepoint) were hierarchically clustered and compared via correlation (Fig. 4a). Samples largely clustered by timepoint, validating the existence of patient-independent molecular signatures. We then validated our dataset against external data from Maus et al., which consisted of CD8⁺ CAR T cells from patients with large B-cell lymphoma (Fig. 4a, b, colored in tan and brown, six in total after filtering)[27]. Based on their sample collection timing (day 7), external data from Maus et al. should resemble our samples at T_{exp}, rather than at T_{per}. Consistent with expectations, external data resembled T_{exp} transcriptomes on both pseudo-bulk (Fig. 4a, via correlation) and single-cell (Fig. 4b, via label transfer) levels, which increases the external validity of our findings.

To elucidate the immunological processes at each timepoint, CD8⁺ CAR T-cell transcriptomes at T_{exp} and T_{per} from our seven patients were compared via GSEA (Fig. 4c and data file S1 for single-cell method, Fig. S9a and data file S2 for pseudo-bulk method) and DGEA (Fig. 4d, Fig. S9b, data file S3-4). CAR T cells at T_{exp} upregulated gene sets for cell cycling and apoptosis, consistent with a short-lived phenotype. Upregulation of the cell cycling gene set remained true even when only comparing the proliferating cell cluster at T_{exp} and T_{per} (Fig. S9d). This indicates that, while proliferating cells are present at both T_{exp} and T_{per}, those at T_{exp} are more proliferative than those at T_{per}. We also observed T_{exp}-specific and cluster-independent upregulation of genes related to T-cell activation (including *CD69*, *CD44*, *CD74*) and exhaustion (including *PRDM1*, *CTLA4*, *NR4A2*), implicating antigen-engagement and CAR-mediated signaling during T_{exp}. On the other hand, CAR T cells at T_{per} upregulated gene sets for cytotoxicity and immune regulation. Expression of cytotoxicity-related genes (including *KLRB1*, *FCGR3A*, *PRF1*, *GZMB*, *NKG7*) was restricted to TE and exhausted-like TE clusters, indicating that this gene signature arises from T_{per}-specific preponderance of the terminal effector phenotype. We also observed T_{per}-specific upregulation of regulatory genes, including GTPase immune-associated proteins (*GIMAP5*, *GIMAP7*) which predict long-term persistence[33], as well as sphingosine-1-phosphate receptors (*S1PR1*, *S1PR5*) which indicate blood localization[34]. These signatures suggest that CAR T cells at T_{per} are functional and capable of long-term persistence in peripheral blood. Lastly, downregulation of genes related to T-cell activation and exhaustion implicate decreased in vivo antigen load and/or CAR-mediated signaling during T_{per}.

Interestingly, some differentially expressed gene signatures between CD8⁺ CAR T cells at T_{exp} and T_{per} pertained to cytokine signaling (Fig. 4c, d, see Fig. S9c). CAR T cells at T_{exp} upregulated TNF response genes (including *NFKBIA*, *NFKBIE*, *DUSP4*, *RELB*). TNF can be secreted by CAR T cells for autocrine signaling[20], predicts efficacious CAR T cells[20], and contributes to CRS[35]. On the other hand, CAR T cells at T_{per} upregulated type I interferon (IFN-I) response genes (including *STAT1*, *IFITM1*, *IFITM2*, *IRF7*). Many IFN-I response genes have known antiviral functions. The temporally specific and cluster-independent upregulation of TNF and IFN-I response genes indicates a dynamic in vivo cytokine environment during the CAR T-cell immune response.

Next, we investigated T_{exp}- and T_{per}-specific regulatory networks using a machine-learning model (Fig. 4e, see Methods). Single-cell transcriptomes were transformed into regulomes to calculate regulon scores. A machine-learning model was trained using the regulon scores to classify CD8⁺ CAR T cells at T_{exp} and T_{per}. This strategy resulted in high (~90%) classification accuracy across patients (Fig. S10a). Top T_{exp}- and T_{per}-determining regulons were identified based on each regulon's importance (SHAP value) for the model's prediction (Fig. 4f, data file S5). Sizes of timepoint-determining regulons span approximately 10–1000 genes (Fig. S10b). Regulon expression was compared between cell clusters and timepoints (Fig. 4g). T_{exp}- and T_{per}-determining regulons were broadly upregulated at T_{exp} and T_{per}, respectively. However, expression of some regulons was cluster-specific (e.g., *FLI1* regulon among EM clusters).

The top three T_{exp}-determining regulons (for *JUND*, *RELB*, *BHLHE40*) exhibited higher expression among non-proliferating clusters and included co-regulated inflammation-associated genes (including *NFKBIA*, *TNFAIP3*, *DUSP5*) (Fig. 4h, see Fig. S11a)[36]. The *RELB*

https://doi.org/10.1038/s41467-025-59298-w

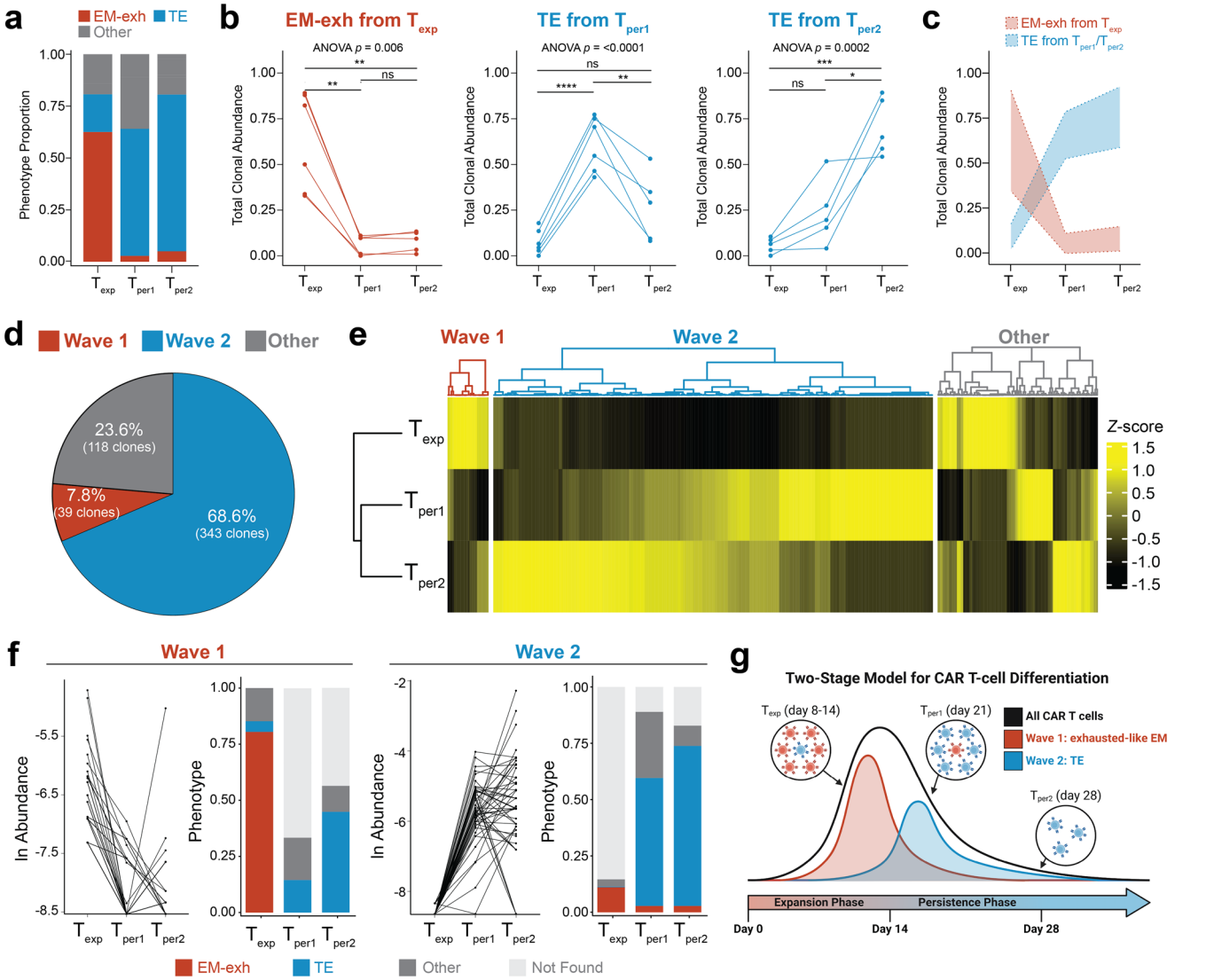

Fig. 3 | Integration of clonotypic and phenotypic shifts supports a two-stage differentiation model. All figure panels are based on the clonotype-phenotype linked dataset ($n = 32432$ cells). **a** Proportion of CAR T cells with an exhausted-like effector memory (EM-exh), terminal effector (TE), or other phenotypes at each timepoint. **b** Total abundance of all clones that were predominantly EM-exh at T_{exp} (left), TE at T_{per1} (middle), or TE at T_{per2} (right), measured across timepoints. A clone's predominant phenotype was defined as the phenotype with the greatest representation. Each point represents clones from a patient ($n = 6$). Abundance across timepoints were compared by repeated measures ANOVA with paired two-sided post hoc *t* tests, whereby **** indicates $p < 0.0001$, *** indicates $p < 0.001$, ** indicates $p < 0.01$, * indicates $p < 0.05$, and ns indicates not significant. **c** Overlay of clonal abundance dynamics with 95% confidence intervals for clones annotated as EM-exh from T_{exp} (red) or TE from T_{per1}/T_{per2} (blue). **d** Pie chart depicting proportion of the top 500 clones classified as Wave 1, Wave 2, or Other. **e** Heatmap depicting normalized CAR abundance across timepoints for the top 500 largest clones. **f** Clonal dynamics and phenotypic distribution for the top 500 clones, grouped into Wave 1 and Wave 2. Left panels depict the change in clonal abundance across timepoints, while right panels show the predominant phenotype distribution at each timepoint. **g** Cartoon summarizing the two-stage model for CAR T-cell differentiation. Bulk CAR T-cell expansion and contraction (black line) masks the dynamics of Wave 1 (EM-exh, expansion phase timeframe, red) and Wave 2 (TE, persistence phase timeframe, blue) clones. Created in BioRender. Hu, Y. (2025) https://BioRender.com/rwp4v6g. Source data are provided as a Source Data file.

and *BHLHE40* genes themselves are included in the *JUND* regulon, indicating they may be directly upregulated by *JUND*. These three regulons were upregulated at T_{exp} and suggest response to pro-inflammatory cytokines (such as TNF, discussed above) or CAR signaling. *BHLHE40* rewires mitochondrial metabolism for tissue residency[37], which may contribute to CAR T-cell fitness after entering the lymphoma. Shared genes between the *JUND* and *BHLHE40* regulons included AP-1 transcription factors (*JUN*, *JUNB*, *FOSL2*), which have been implicated in T-cell and CAR T-cell exhaustion[38,39], and may contribute to the exhausted-like EM phenotype that predominates the first clonal wave at T_{exp}. Among remaining T_{exp}-determining regulons, *FLI1* is notable for antagonizing effector T-cell differentiation[40]. Consistent with known biology, expression of the *FLI1* regulon was upregulated among EM clusters, downregulated among TE clusters, and did not significantly change between T_{exp} and T_{per} within TE clusters.

On the other hand, T_{per}-determining regulons were more obscure (Fig. 4i, see Fig. S11b). Among top T_{per}-determining regulons, *KLF13* regulates T-cell apoptosis[41], *BPTF* activates a stemness gene expression program[42] and maintains peripheral T-cell homeostasis[43], and *ELF4* promotes memory $CD8^+$ T cells by regulating quiescence[44]. Altogether, the putative functions of the *KLF13*, *BPTF*, and *ELF4* regulons may underlie the delayed expansion and persistence of the second clonal wave at T_{per}. Moreover, these functions indicate restoration of immune homeostasis during T_{per}. The *TBX21* regulon was notable for effector-associated genes (including *NKG7*, *ZEB2*) and was upregulated

https://doi.org/10.1038/s41467-025-59298-w

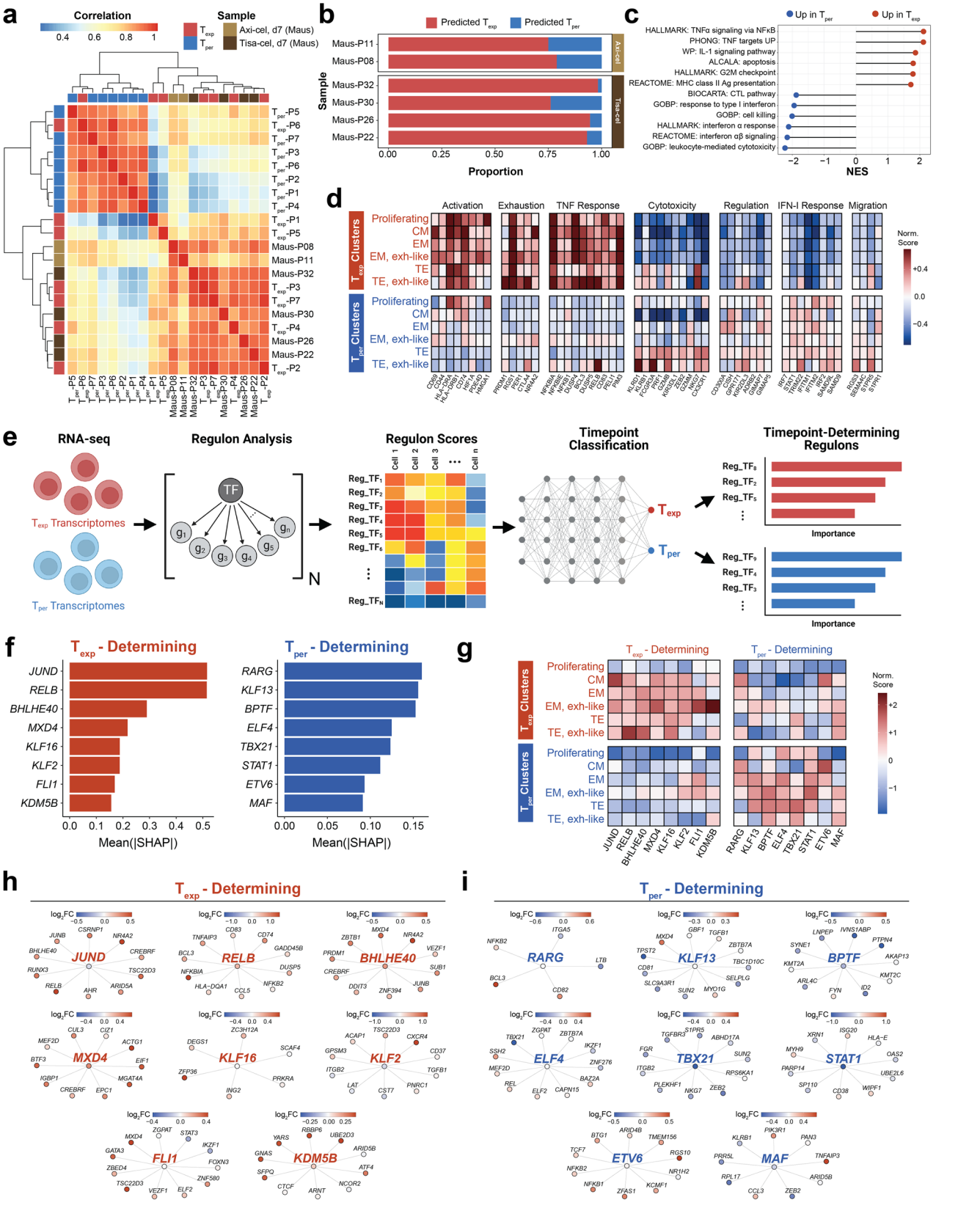

within non-CM clusters, consistent with preponderance of the TE phenotype at T_{per}. The *TBX21* regulon also includes *S1PR5*, which is a known T-BET target[45] and retains T cells in peripheral blood[34]. Lastly, the *STAT1* regulon was notable for interferon-associated antiviral genes (including *OAS2*, *ISG20*), in concordance with upregulation of IFN-I signaling gene sets at T_{per}.

CD8$^+$ CAR T cells at T_{exp} and T_{per} originate from distinct precursors in the infusion product

The distinct clonotypes, phenotypes, transcriptional signatures, and regulatory networks underlying the two waves of CD8$^+$ CAR T cells led us to hypothesize that they originate from distinct precursors in the infusion product. To test this hypothesis, we first investigated infusion

Fig. 4 | Transcriptional signatures and regulatory networks of CD8⁺ CAR T cells at T_{exp} and T_{per}. **a** Heatmap depicting correlation between pseudo-bulk transcriptome of each sample (patient by timepoint). Samples were ordered along columns and rows by hierarchical clustering. Transcriptomes of day 7 samples from Maus et al. were added for external validation. **b** Stacked bar graph depicting label transfer of timepoint (T_{exp} or T_{per}) from this study's dataset onto single-cell transcriptomes of samples from Maus et al. **c** Gene set enrichment analysis comparing CAR T cells between T_{exp} and T_{per}. Gene sets were ordered by direction of upregulation and magnitude of enrichment. **d** Tile map depicting normalized expression of genes (columns) among different cell clusters at T_{exp} and T_{per} (rows). Genes were manually grouped into modules according to known functions. **e** Schematic for regulon construction and T_{exp} versus T_{per} classification. After transcriptomes were transformed into regulomes, regulon scores were calculated to train a machine-learning model to classify CAR T cells from T_{exp} and T_{per}. Key regulons were identified based on importance for the model's predictions. Created in BioRender. Hu, Y. (2025) https://BioRender.com/3ltrr3g. **f** Bar graph depicting the SHapley Additive exPlanation (SHAP) values for the top eight regulons underlying T_{exp} and T_{per} predictions. **g** Tile map depicting normalized signature scores of regulons (columns) among different cell clusters at T_{exp} and T_{per} (rows). Regulons were grouped as T_{exp}-determining (left) and T_{per}-determining (right). Target networks for the top eight T_{exp}-determining (**h**) and T_{per}-determining regulons (**i**). In each regulatory network, only the top differentially expressed genes are depicted. Each gene is colored according to $\log_2$ fold-change between expression in T_{exp} (red) and T_{per} (blue). Source data are provided as a Source Data file.

product phenotypes. After filtering for infusion product CD8⁺ T cells, we identified four clusters based on gene expression density (Fig. 5a, b, Fig. S12b) and levels (Fig. 5c, Fig. S12a): proliferating (high *MKI67*), activated naïve-like (naïve-act, high *TCF7*), type 1 effector (EFF-Tc1, high *TBX21*), and type 2 effector (EFF-Tc2, high *GATA3*) T cells. The *TCF7*^{hi} naïve-act cluster upregulated markers of naiveness (*IL7R*, *LEF1*, *CCR7*, CD45RA) and T-cell activation (*CD38*, *CD95*), consistent with an early activated or stem cell-like memory phenotype. The two EFF clusters upregulated cytolytic molecules (*GZMB*, *PRF1*, *GNLY*) and downregulated markers of naiveness (*IL7R*, *LEF1*). EFF-Tc1 and EFF-Tc2 were distinguished by expression density of lineage-specific transcription factors (*TBX21* for Tc1, *GATA3* for Tc2) and receptors (*KLRG1* for Tc1, *CCR4* for Tc2). The EFF-Tc1 cluster exhibited lower CAR transgene expression than the EFF-Tc2 cluster (Fig. S12b, c), which may impact their functional phenotypes in vivo[46,47]. The three non-proliferating clusters upregulated *IRF7* and anti-viral genes (*ISG20*, *IFITM1*, *IFITM2*), indicating type I interferon signaling during ex vivo transduction and/or expansion. Cluster proportions varied between patients (Fig. S12d). In general, proliferating T cells (54%) were the most prevalent, while proportions of non-proliferating phenotypes (naïve-act, 14%; EFF-Tc1, 11%; EFF-Tc2, 21%) were mutually comparable (Fig. 5e, top row).

Having established infusion product phenotypes, we next performed TCR lineage tracing analysis to developmentally link infusion product CAR T cells with peripheral blood CAR T cells using their endogenous TCR clonotypes as unique indices. This method delineates infusion product precursors of CD8⁺ CAR T cells at T_{exp} ("Pre-T_{exp}") and at T_{per} ("Pre-T_{per}") (Fig. 5d). Both Pre-T_{exp} and Pre-T_{per} comprised all four infusion product clusters (Fig. 5e, bottom rows) and largely overlapped on the UMAP (Fig. 5f). Hence, we conclude that coarse cluster phenotype alone cannot accurately predict in vivo differentiation. Compared to T cells not linked to peripheral blood ("IP only"), Pre-T_{exp} and Pre-T_{per} cells upregulated expression of effectorness (including *GZMB*, *TNF*, *GNLY*) and type 1 polarization (including *IFNG*, *KLRG1*) genes, as well as lower expression of stemness (including *SELL*, *IL7R*) and type 2 polarization (including *GATA3*, *IL4R*) genes (Fig. 5g). The significance of type 1 versus type 2 polarized CD8⁺ CAR T cells is not well-understood in the literature and warrants future studies. Pathway analysis indicated that Pre-T_{exp} and Pre-T_{per} upregulated gene sets for T-cell effector function ("PD-1 signaling", "T-cell-mediated cytotoxicity"), response to interferon γ ("interferon γ signaling", "antigen processing and presentation"), and DNA replication, whereas non-linked CAR T cells upregulated gene sets for stemness (Fig. 5h, data file S6). Our discovery of CD8⁺ CAR T-cell precursors with an effector-like phenotype is corroborated by findings from Thomas et al., who also identified effector-like precursors from CAR T-cell patients treated for B-cell acute lymphoblastic leukemia[48]. Possible fates for the non-linked, naïve-like, IP-only CAR T cells include extravasation into the lymphoma, expansion in peripheral blood outside the T_{exp}-T_{per} window (day 8–28), or failure to persist in vivo.

Lastly, we directly compared transcriptomic signatures of Pre-T_{exp} and Pre-T_{per} via GSEA. Although both Pre-T_{exp} and Pre-T_{per} broadly exhibited an effector phenotype (Fig. 5g, h), Pre-T_{exp} upregulated effectorness-associated gene sets (including TCR, PD-1, interferon γ, and IL-1 signaling), whereas Pre-T_{per} upregulated stemness-associated gene sets (Fig. 5i). In concordance, DGEA showed that Pre-T_{exp} upregulated effector molecules (*GZMB*, *GZMK*, *FCGR3A*, *NKG7*, *KLRG1*), AP-1 transcription factors (*JUN*, *JUND*, *FOS*), and MHC class II expression (*HLA-DRB1*, *HLA-DRB5*, *HLA-DRA*), whereas Pre-T_{per} upregulated naïve-like markers (*SELL*, *IL7R*, *S1PR1*) (Fig. S12e, data file S7). Upregulation of *JUN* in Pre-T_{exp} confers exhaustion resistance[38], potentially underlying their eventual efficacy at T_{exp}. Interestingly, Pre-T_{per} exhibited greater CAR transgene expression (Fig. S12e), which may reflect transduction differences among apheresis precursors or a link between CAR expression and in vivo differentiation[47]. Next, we compared Pre-T_{exp} and Pre-T_{per} using transcriptomic signatures from a human CD8⁺ differentiation atlas from Giles et al.[49]. Pre-T_{exp} more closely resembled an effector memory state, whereas Pre-T_{per} more closely resembled either a stem-cell memory or central memory state (Fig. 5j). Altogether, these patterns indicate that, while both Pre-T_{exp} and Pre-T_{per} exhibited an effector phenotype in the infusion product, Pre-T_{exp} were more differentiated with greater effectorness, whereas Pre-T_{per} were less differentiated with greater stemness.

In conclusion, TCR lineage tracing analysis supports our hypothesis that CD8⁺ CAR T cells at T_{exp} and T_{per} originate from different infusion product precursors. Integrating these findings into the two-stage differentiation model paints a more complete picture of CD8⁺ CAR T cells over the month following CAR T-cell administration (Fig. 5k). Effector CD8⁺ CAR T cells exist along a gradient of effectorness and stemness in the infusion product. Following infusion into the patient, effector CAR T cells with greater effectorness rapidly expand until peak expansion (T_{exp}, days 8–12), adopting a functional and cytotoxic EM phenotype with exhaustion-like characteristics upon antigen stimulation. Lymphoma infiltration and in vivo killing[50], CRS[5], and ICANS[5] coincide with the T_{exp} timeframe, suggesting that these CAR T cells mediate tumor clearance and side effects. Subsequently, this first wave of expanded CAR T cells diminishes through apoptosis or extravasation. Simultaneously, the remaining effector CAR T cells with greater stemness from the infusion product expand during the post-peak persistence timeframe (T_{per}, day 21–28). These newer and longer-lived CAR T cells adopt effector characteristics and persist in vivo, where they may ensure a durable response through long-term immunosurveillance.

CD8⁺ Exhausted-like EM CAR T cells at T_{exp} exhibit characteristics of early exhaustion

Discovery of the predominant exhausted-like EM phenotype in peripheral blood at T_{exp} may be surprising since exhaustion was conventionally defined in lymphoid organs or tumor-infiltrating lymphocytes[51]. To verify this annotation, we further characterized the molecular signatures of the exhausted-like EM cluster. The exhausted-like EM cluster was densely situated at the lower half of the UMAP (Fig. 6a, b). We used RNA-seq/CITE-seq to examine gene and protein expression density, respectively (Fig. 6c, Fig. S13a for additional

https://doi.org/10.1038/s41467-025-59298-w

markers). The exhausted-like EM cluster highly expressed exhaustion-associated transcription factors (*NR4A2*, *TOX*, *IRF4*) and inhibitory receptors (*ENTPD1*, *PDCD1*, *TIGIT*, *LAG3*, *CTLA4*). Intermediate expression of memory (*TCF7*, *LEF1*, *CD27*, *IL7R*) and effector (*TBX21*, *GZMB*, *PRF1*, *GNLY*, *IFNG*, *NKG7*) genes was also observed. Additionally, the cluster exhibited low expression of *CX3CR1* (effector lineage marker) and *B3GAT1* (senescence marker). CITE-seq measurements of protein expression for cell surface receptors (including CD39, PD-1, TIGIT, LAG3, CD27, CD57, CD127, TIM-3, CXCR3) were largely consistent with corresponding gene expression. Sequencing data indicated that high expression of CD39 (protein for *ENTPD1*) and low expression of CD57 (protein for *B3GAT1*) most clearly differentiated the exhausted-like EM

Fig. 5 | Infusion product precursors of peripheral blood CD8⁺ CAR T cells. **a** UMAP depicting single-cell transcriptomes of infusion product CD8⁺ T cells colored by cell cluster. Density maps (**b**) and violin plots (**c**) depicting expression levels of key genes and proteins for annotation and phenotyping. For extended version, see Fig. S11a, b. **d** Cartoon depicting identification of Pre-T_{exp} and Pre-T_{per} using endogenous TCR clonotypes as unique indices. Created in BioRender. Hu, Y. (2025) https://BioRender.com/49klewt. **e** Stacked bar graph depicting proportion distribution of all infusion product (top row) or precursors of peripheral blood CD8⁺ CAR T cells (bottom two rows) among the four cell clusters. **f** Colored UMAPs depicting distribution of Pre-T_{exp}, Pre-T_{per}, and non-linked infusion product cells ("IP only") on the overall UMAP. **g** Tile map depicting normalized expression of genes (columns) among Pre-T_{exp}, Pre-T_{per}, and IP only infusion product cells (rows). Genes were manually grouped into modules according to known functions. **h** Violin plots depicting expression levels of select differentially expressed gene sets between Pre-T_{exp} ($n = 1813$ cells), Pre-T_{per} ($n = 2502$ cells), and IP only ($n = 8464$ cells) infusion product cells. Expression levels were compared by two-sided Wilcoxon Rank-Sum test with p values adjusted for multiple hypotheses testing using the Benjamini-Hochberg method, whereby **** indicates $p < 0.0001$ and ** indicates $p < 0.01$. The central line indicates the median. The bounds of the box indicate the 25th–75th percentile. The length of the whiskers indicates 1.5 times the inter-quartile range from the first and third quartiles. **i** Gene set enrichment analysis comparing Pre-T_{exp} and Pre-T_{per}. Gene sets were ordered according to direction of upregulation and magnitude of enrichment. **j** Enrichment plots for select gene sets differentially expressed between Pre-T_{exp} and Pre-T_{per} infusion product cells. Enrichment scores are computed by the Kolmogorov-Smirnov test with false discovery rate (FDR) adjusted q-values. **k** Cartoon depicting fates of CD8⁺ CAR T cells over the entire course of therapy, from infusion product precursors to peripheral blood CAR T cells at T_{exp} and T_{per}. Created in BioRender. Hu, Y. (2025) https://BioRender.com/3dtq7c4. NES normalized enrichment score. Source data are provided as a Source Data file.

cluster from other clusters. To validate these characteristics, flow cytometry was employed to analyze a set of longitudinal patient PBMCs (Fig. S13b for gating). Consistent with sequencing data, flow cytometry data demonstrated that the CD39⁺CD57⁻ phenotype was highest among CD8⁺ CAR T cells at T_{exp} (75%) compared to at T_{per1} (33%) and T_{per2} (18%) (Fig. 6d, top row). Furthermore, flow cytometry showed decreased CX3CR1 expression at T_{exp}, and increased expression at T_{per1} and T_{per2}, in agreement with sequencing data (Fig. 6d, bottom row). This mixed expression pattern of exhaustion, memory, and effector markers resembles the circulating PD1⁺CD39⁺ T_{ex} cells described by the Wherry group's human T-cell differentiation atlas[49].

Next, we conducted GSEA using gene sets from Wherry et al. that identified T-cell differentiation states in the Armstrong/clone 13 LCMV model (Fig. 6e).[52] These gene sets constitute comprehensive references for defining T-cell exhaustion because they (1) incorporate standing knowledge from the entire field, (2) integrate single-cell RNA-seq and ATAC-seq data from serial timepoints, and (3) originate from the Wherry group where comprehensive transcriptional signatures of T-cell exhaustion and most exhausted subsets were first defined. The two EM clusters (EM and exhausted-like EM) in our dataset correlated with different states from the Wherry group's model. Our EM cluster resembled the "transitional I" T cells from the Armstrong model, indicating that these cells are not exhausted. Conversely, our exhausted-like EM cluster resembled the "precursor exhausted" T cells from the clone 13 model (Fig. 6f, left). Simultaneously, the exhausted-like EM cluster did not resemble the "terminally exhausted" T cells from the same model (Fig. 6f, right), which instead correlated with our exhausted-like TE cluster. Given clear differences between the EM and exhausted-like EM clusters, we directly compared their transcriptomic signatures through DGEA and GSEA. The exhausted-like EM cluster upregulated genes associated with T-cell activation (*CD69*, *CD38*, *DUSP4*, *NFKBIA*) and exhaustion (*TOX*, *NR4A2*, *PRDM1*, *CTLA4*) (Fig. 6g, data file S8). In contrast, the EM cluster upregulated genes associated with effector function (*TBX21*, *CX3CR1*, *GZMB*, *PRF1*, *FCGR3A*), memory (*IL7R*, *S1PR1*), and type I interferon signaling (*STAT1*, *IFITM1*, *IFITM3*). GSEA revealed that the exhausted-like EM cluster exhibited more exhaustion signatures and fewer effector signatures compared to the EM cluster (Fig. 6h, left column, Fig. S13c). GSEA also confirmed that the exhausted-like EM cluster resembled the "exhausted progenitor" and "exhausted precursor" subsets from Wherry et al. (whereas the EM cluster resembled the "transitional I" subset) (Fig. 6h, middle and right columns). Our findings suggest that the exhausted-like EM cluster exhibits robust gene and protein signatures of early exhaustion (justifying the "exhausted-like" annotation), yet is also phenotypically distinct from effector memory T cells.

Discussion

In this study, we use a combination of single-cell RNA-seq/CITE-seq/TCR-seq and longitudinal analyses to investigate CD28-costimulated CAR T-cell differentiation in seven patients with r/r DLBCL. Our findings are summarized in our two-stage model for CAR T-cell differentiation (Fig. 3g). Specifically, CD8⁺ CAR T cells undergo two distinct clonal expansion waves (at peak expansion and post-peak persistence timeframes), as revealed by clonotypic, phenotypic, and linked clonotypic-phenotypic analyses. The two waves are dominated by exhausted-like effector memory and terminal effector phenotypes, respectively. The exhausted-like effector memory annotation is supported by a CD39⁺CD57⁻ flow phenotype, low CX3CR1 expression, and an early exhaustion signature. We also identify transcription factors and regulatory networks associated with the first wave (including *JUND*, *RELB*, *BHLHE40*, *FLI1* regulons) and second wave (including *KLF13*, *BPTF*, *ELF4*, *TBX1*, *STAT1* regulons). Lastly, lineage tracing analysis determined that CD8⁺ CAR T cells from both waves derive from effector precursors in the infusion product. However, effector precursors of the first wave exhibit more effector-like signatures, whereas effector precursors of the second wave exhibit more stem-like signatures (Fig. 5k), suggesting that pre-infusion heterogeneity mediates two-stage differentiation. Our two-stage model implies that manipulating the phenotypic composition of the infusion product may allow more precise control over in vivo CAR T-cell differentiation for modulating therapeutic efficacy.

Although two-stage differentiation is a phenomenon that has not yet been reported in the literature, the individual elements of our model are consistent with current understanding in the field. Previous studies on 4-1BB-costimulated CAR T-cell differentiation described bursts of CAR T-cell clonal expansion that lead to significant changes in the CAR T-cell clonal repertoire over time[19,53]. Our study not only generalizes this observation to CD28-costimulated CARs, but also directly pairs changes in the clonal repertoire with changes in T-cell phenotypes. Furthermore, previous reports have described CAR T-cell clones with memory-like phenotypes that exhibit delayed expansion after infusion[23], which corroborates with the second clonal expansion wave at T_{per}. Finally, the T_{exp}- and T_{per}-specific phenotypes described in our model are consistent with prior phenotyping studies[25,27,48,54,55]. We also report agreement between our transcriptomes at T_{exp} and external data from Maus et al.[27]. By integrating our findings from multiple data modalities with established studies in the CAR T-cell field, we present a more complete and coherent two-stage model for in vivo CD28-costimulated CAR T-cell differentiation.

The two-stage differentiation model we present in this study has an important implication. CD28-costimulated CD8⁺ CAR T cells from the peak expansion and post-peak persistence timeframes are biologically uncoupled. This uncoupling significantly informs how we understand CAR T-cell expansion and persistence. Expansion facilitates rapid tumor clearance but can also cause CRS and ICANS[5,17], while persistence facilitates long-term immunosurveillance but can also cause B-cell aplasia and hypogammaglobulinemia[9,13,56]. Our findings suggest that expansion and persistence, both of which serve

https://doi.org/10.1038/s41467-025-59298-w

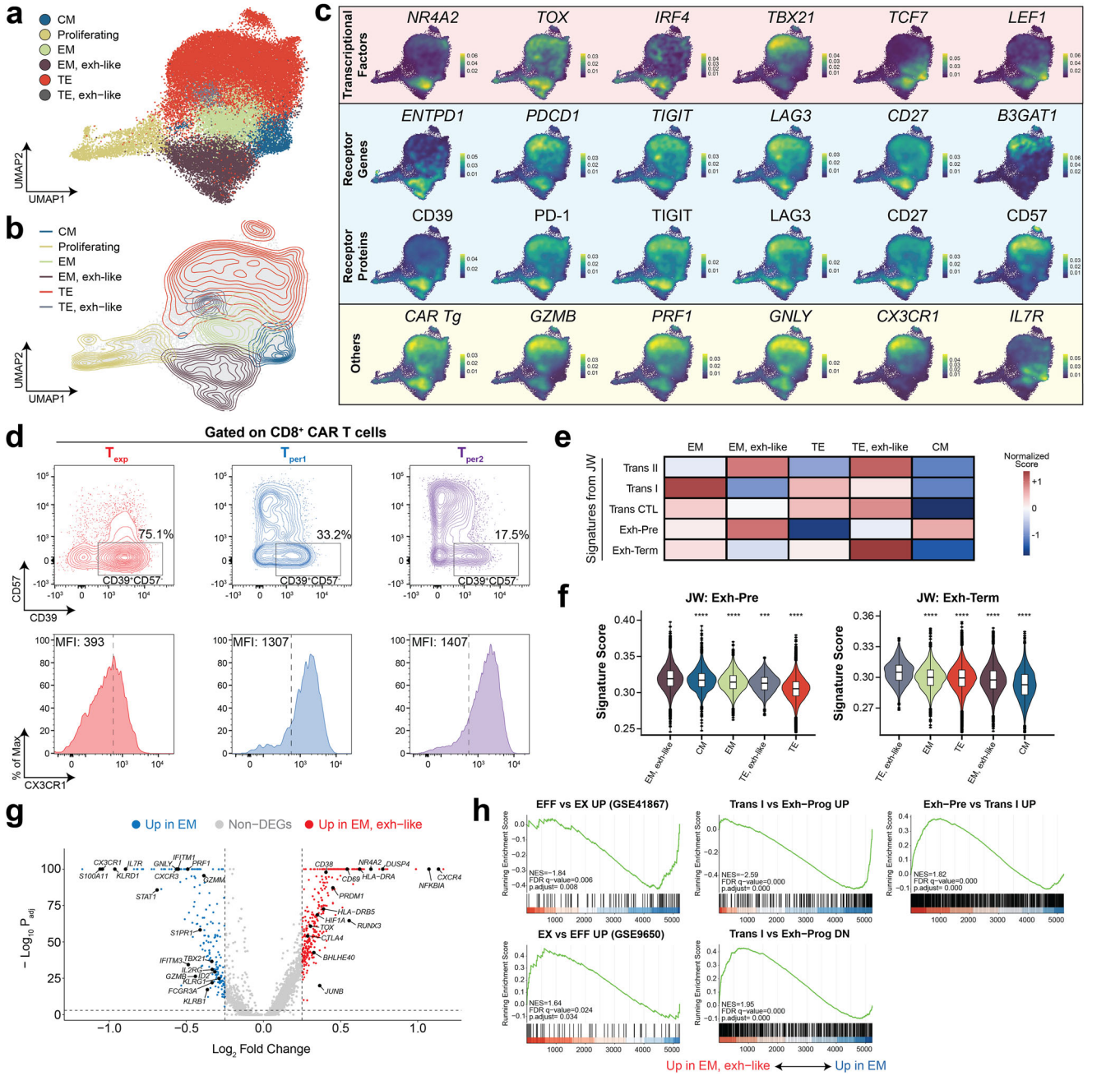

Fig. 6 | Transcriptomic signatures of exhausted-like EM CD8⁺ CAR T cells. UMAP depicting single-cell transcriptomes of peripheral blood CD8⁺ T cells colored by cell cluster (**a**) or density contours of each cluster (**b**). The exhausted-like EM cluster is located on the lower half of the UMAP. **c** Density maps depicting expression levels of major T-cell genes and proteins, divided into categories. In the "receptor" category, proteins are placed directly beneath the corresponding gene. **d** Flow plots for validating transcriptomic data. Plots depict expression of CD39 and CD57 (top row) or CX3CR1 (bottom row) in CD8⁺ CAR T cells at each timepoint from P2. Exhausted-like EM CAR T cells were expected to be T_{exp}-specific with high CD39 and low CD57/CX3CR1 expression. **e**, **f** Heat map depicting normalized expression of major gene sets from Wherry et al. (**e**). Expression of two of the gene sets were depicted as violin plots (**f**), ordered by decreasing expression level per cluster (EM, exh-like: $n = 7163$ cells; CM: $n = 1883$ cells, EM: $n = 4937$ cells; TE, exh-like: $n = 552$ cells; TE: $n = 21019$ cells). The central line indicates the median. The bounds of the box indicate the 25th–75th percentile. The length of the whiskers indicates 1.5 times the inter-quartile range from the first and third quartiles. Expression levels were compared to that of the cluster with highest expression via two-sided Wilcoxon Rank-Sum test, with p values adjusted for multiple hypotheses testing using the Benjamini-Hochberg method, whereby **** indicates $p < 0.0001$, *** indicates $p < 0.001$. **g** Volcano plot depicting differentially expressed genes found via two-sided Wilcoxon Rank-Sum test with Bonferroni adjustment between EM and exhausted-like EM CD8⁺ CAR T cells. Genes were colored according to direction of upregulation. **h** Enrichment plots for select gene sets differentially expressed between EM and exhausted-like EM CD8⁺ CAR T cells. Enrichment scores are computed by the Kolmogorov-Smirnov test with false discovery rate (FDR) adjusted q-values. Source data are provided as a Source Data file.

complementary clinical purposes, are mediated by distinct CD8⁺ CAR T-cell populations. Effective and personalized CAR T-cell therapies balance expansion and persistence, taking into consideration each patient's tumor burden, tolerance for side effects, and risk of relapse. Our findings suggest that expansion and persistence may be independently tuned to meet a patient's needs. On the other hand, our findings also suggest that engineering CD8⁺ CAR T cells that simultaneously expand and persist competently may be challenging, given that these characteristics originate from uncoupled CAR T-cell populations in vivo.

In addition to clonal kinetics and phenotypic heterogeneity, we characterized T_{exp}- and T_{per}-specific upregulation of TNF and IFN-I response gene sets and regulons, respectively. Notably, TNF-secreting $CD8^+$ CAR T cells have been associated with complete responders[20], suggesting that TNF may be signaling in an autocrine or paracrine manner during T_{exp}. Upregulation of IFN-I response genes during T_{per} was intriguing. IFN-I response signatures in the apheresis of patients with B-cell acute lymphoblastic leukemia predict poor CAR T-cell persistence[57], but IFN-I signaling may also enhance CAR T-cell efficacy in vivo[58]. Complicating this story further, we also identified IFN-I response signatures in the infusion product, which implies that interferons are secreted by an unknown source during ex vivo transduction and/or expansion. Hence, the possible roles of IFN-I in CAR T-cell differentiation are likely complex, context-dependent, or time-dependent, and warrant further mechanistic investigation.

We concluded our study by using single-cell TCR-seq to link $CD8^+$ CAR T cells at T_{exp} and T_{per} with effector precursors in the infusion product that exhibit more effector-like or more stem-like signatures, respectively. Discovery of effector precursors is externally corroborated by findings from Thomas et al.[48]. Importantly, this linkage suggests that the magnitude or duration of peak expansion and post-peak persistence can be modulated by manipulating the relative quantities of precursors in the infusion product. However, we cannot rule out the possibility that the in vivo peripheral blood environment in a patient with DLBCL also plays an instrumental role in determining whether a CAR T cell clonally expands at T_{exp} or T_{per}. Future studies can investigate this possibility by analyzing interactions between CAR T cells and other blood cells (such as myeloid cells, B cells, or NK cells) at T_{exp} and T_{per}.

The present study focuses on CD28-costimulated CAR T cells from complete responders, but two-stage differentiation may be more widely applicable. Others forms of adoptive cell therapy, such as 4-1BB-costimulated CAR T cells for B-cell leukemias[59] or systemic lupus erythematosus[60], may also exhibit a two-stage differentiation pattern in vivo. Indeed, our transcriptomic signatures at T_{exp} were highly consistent with external data from day 7 tisagenlecleucel $CD8^+$ CAR T cells from Maus et al[27], hinting that two-stage differentiation may be more general. Different forms of adoptive cell therapy and disease contexts may exhibit different temporal dynamics or favor one wave over the other. Two-stage differentiation may also be aberrant in non-responders. Future studies are needed to explore potential differences in temporal dynamics, cell phenotypes, or major regulatory pathways at longitudinal timepoints in alternative therapeutic contexts.

Although this current study represents an advance for the CAR T-cell therapy field, we acknowledge four limitations. Firstly, we analyzed CAR T cells in two locations: peripheral blood and infusion product. However, CAR T cells are also found elsewhere, including lymph nodes and lymphoma foci. Importantly, CAR T-cell differentiation may be influenced by interactions with antigen-presenting cells in lymph nodes or with tumor cells in the lymphoma. Our study was ultimately limited by sample availability. Future studies can focus on less accessible locations and determine CAR T cell fates beyond peripheral blood. Secondly, we studied CAR T-cell intrinsic factors (RNAs, proteins, clonotypes) that can influence differentiation. However, differentiation may also depend on interactions between CAR T cells and a complex in vivo environment that includes other leukocytes (myeloid cells, B cells, NK cells), lymphoma cells, and cytokines. Thirdly, we focused on CAR T cells longitudinally between peak expansion and post-peak persistence timeframes. Hence, we cannot rule out additional waves of clonal expansion in the near (<1 week after infusion) or long (>1 month after infusion) terms. Lastly, we lack knowledge on whether two-stage differentiation applies to other contexts, such as non-responders, 4-1BB-costimulated CAR T cells, or TCR-transduced T cells. Future studies can explore alternative clinical contexts and test the generality of the two-stage differentiation model.

Methods

All methods complied with ethical guidelines established by the institutional review board at the University of Chicago Medicine.

Patient biospecimen collection

Deidentified biospecimens were obtained from a cellular therapy biobank in accordance with the institutional review board at the University of Chicago Medicine. Consent was obtained for biospecimen collection. Ethical guidelines were followed.

Longitudinal peripheral blood mononuclear cells (PBMCs) were collected from peripheral blood biospecimens by Ficoll-Paque PLUS (Cytiva, 95021-205) and stored in freezing media (RPMI, 10% FBS, 10% DMSO). Residual infusion product cells were collected from the patient's spent infusion product bag and stored in CELLBANKER 1 (Amsbio, 11888). Cells were cryopreserved in liquid-phase nitrogen.

Generation of CD19-tetramers

Tetramers[28] were constructed from AviTag-biotinylated human His-tagged CD19 (Acro Biosystems, CD9-H82E9) and Alexa Fluor 647-labeled streptavidin (BioLegend, 405237). Biotinylated CD19 was added to the tetrameric streptavidin at a 4:1 molar ratio for 30 min at 4 °C in the dark. This mixture was diluted with PBS to convenient concentrations for staining. For each batch of biotinylated CD19, quality controls were performed by generating CD19-tetramers and quantifying their ability to stain anti-CD19 CAR-transduced Jurkat T cells.

Single-cell RNA-seq/CITE-seq/TCR-seq

Cryopreserved biospecimens were thawed (RPMI, 10% FBS) and washed with cold FACS buffer (PBS, 2% BSA, 0.05% sodium azide). Fc receptors were blocked with Human TruStain FcX (BioLegend, 422301) at 1:50 dilution for 5 min at 4 °C. Then, cells were incubated for 30 min at 4 °C in the dark with a staining solution containing CITE-seq antibodies (described below), BV421-labeled anti-CD3ε (clone SK7, BioLegend, 344833), and AF647-labeled CD19-tetramers (3 nM final concentration) for CAR T-cell phenotyping and detection. Subsequently, stained cells were conjugated with LIVE/DEAD Fixable Near-IR viability dye (Invitrogen, L34975) at 1:1000 dilution in PBS for 5 min at room temperature. Finally, cells were washed three times in cold cell media (RPMI, 10% FBS) before fluorescence-activated cell sorting (BD Biosciences, FACSAria Fusion). CAR^+ sorting gates were drawn based on fluorescence of PBMCs from a similarly stained healthy donor.

Sorted endogenous T cells ($CD3^+CAR^-$) and CAR T cells ($CD3^+CAR^+$) were separately partitioned into droplets for single-cell RNA-seq/CITE-seq/TCR-seq via Chromium Next GEM Single-Cell 5'Kit v2 (10x Genomics, 1000263). RNA-seq libraries were prepared according to manufacturer protocols. CITE-seq libraries were prepared via the 5' Feature Barcode Kit (10x Genomics, 1000256). TCR-seq libraries were prepared via the Chromium Single-Cell Human TCR Amplification Kit (10x Genomics, 1000252). All libraries (RNA-seq, CITE-seq, TCR-seq) were quantified via the Qubit dsDNA HS Assay Kit (Invitrogen, Q32851), quality-checked for fragment sizes via high-sensitivity D5000 screentapes (Agilent, 5067-5592), pooled, and sequenced (Illumina, Novaseq-6000 and Nextseq-550).

CITE-seq antibody preparation

Thirty-one human "Cellular Indexing of Transcriptomes and Epitopes by Sequencing" (CITE-seq[61]) antibodies were obtained from BioLegend (TotalSeq-C reagents): anti-CD3ε (clone UCHT1, 300479), anti-CD5 (clone UCHT2, 300637), anti-TCRα/β (clone IP26, 306743), anti-TCRγ/δ (clone B1, 331231), anti-CD4 (clone SK3, 344651), anti-CD8α (clone SK1, 344753), anti-CD45RA (clone HI100, 304163), anti-CD45RO (clone UCHL1, 304259), anti-CCR7 (clone G043H7, 353251), anti-CD95 (clone DX2, 305651), anti-CD57 (clone QA17A04, 393321), anti-CD25 (clone BC96, 302649), anti-CD127 (clone A019D5, 351356), anti-CD103 (clone

Ber-ACT8, 350233), anti-CXCR3 (clone G025H7, 353747), anti-CCR4 (clone L291H4, 359425), anti-CCR6 (clone G034E3, 353440), anti-PD-1 (clone EH12.2H7, 329963), anti-TIM-3 (clone F38-2E2, 345049), anti-LAG-3 (clone 11C3C65, 369335), anti-CD39 (clone A1, 328237), anti-TIGIT (clone A15153G, 372729), anti-CD27 (clone O323, 302853), anti-CD40L (clone 24-31, 310849), anti-GITR (clone 108-17, 371227), anti-OX40 (clone Ber-ACT35, 350035), anti-4-1BB (clone 4B4-1, 309839), anti-CD28 (clone CD28.2, 302963), mouse IgG1-κ isotype control (clone MOPC-21, 400187), mouse IgG2a-κ isotype control (clone MOPC-173, 400293), and mouse IgG2b-κ isotype control (clone MPC-11, 400381). All antibodies were diluted at a 1:100 ratio. Residual infusion product cells were stained with all 31 CITE-seq antibodies. Patient peripheral blood mononuclear cells were stained with all CITE-seq antibodies minus anti-CD3ε (30 in total) because T cells sorted from these samples were stained with BV421-labeled anti-CD3ε. To prepare the CITE-seq staining solution, the antibody pool was constructed and centrifuged at 14,000 × *g* for 10 min at room temperature in FACS buffer (PBS, 2% BSA, 0.05% sodium azide) to remove aggregates. The antibody supernatant was extracted and diluted with fresh FACS buffer to appropriate staining concentrations.

Analysis of CAR T-cell phenotype by flow cytometry

Cryopreserved biospecimens were thawed (RPMI, 10% FBS) and washed with cold FACS buffer (PBS, 2% BSA, 0.05% sodium azide). Fc receptors were blocked with Human TruStain FcX (BioLegend, 422301) at 1:50 dilution for 5 min at 4 °C. Then, cells were incubated for 30 min at 4 °C in the dark with a staining solution containing AF647-labeled CD19-tetramers (3 nM final concentration), BV421-labeled anti-CD3ε (clone SK7, BioLegend, 344833), AF488-labeled anti-CD8α (clone SK1, BioLegend, 344716), PE-labeled anti-CX3CR1 (clone 2A9-1, BioLegend, 341603), PE/Cy7-labeled anti-CD39 (clone A1, BioLegend, 328211), and BV605-labeled anti-CD57 (clone QA17A04, BioLegend, 393303). Subsequently, stained cells were conjugated with LIVE/DEAD Fixable Near-IR viability dye (Invitrogen, L34975) at 1:1000 dilution in PBS for 5 min at room temperature. Finally, cells were washed three times in cold FACS buffer (RPMI, 10% FBS) before flow cytometer analysis (BD Biosciences, FACSAria Fusion).

Single-cell RNA-seq data processing

RNA-seq and paired CITE-seq reads were aligned to the GRCh38 reference genome, which was modified with the CAR transgene sequence used in axicabtagene ciloleucel, and quantified using the cellranger count (10x Genomics, version 7.0.0)[62]. Only filtered gene/feature-barcode matrices that contained barcodes with unique molecular identifier (UMI) counts that passed the quality control were used for downstream analyses.

UMAP analysis and clustering on single-cell RNA-seq data

UMAP analysis and clustering were performed using the Seurat package (Version 4.3.0)[63]. Raw count matrices were first converted to Seurat objects before being further merged into one Seurat object, with protein expression added as the antibody-derived tag (ADT) assay. Cells with <300 genes detected or >10% mitochondrial RNA content were excluded from further analysis.

The raw count was log-normalized using the *NormalizeData* function with default options. The top 5000 variable features were then identified using the *FindVariableFeatures* function with the default "vst" method. The data were centered and scaled using the *ScaleData* function, with additional regression against 1) the percent of mitochondrial RNA content and 2) difference in cell cycle S-phase score and G2M-phase score. Scaled data were then used as input for principal component analysis (PCA) based on variable genes using the *RunPCA* function. Data harmonization to remove patient-specific effects was performed on the principal components using the Harmony package (Version 1.0) through the *RunHarmony* function[64]. Next, UMAP was constructed based on the first 30 harmony components. The same harmony components were used to construct the shared nearest neighbor (SNN) graph using the *FindNeighbors* function, which was then partitioned to identify clusters using the *FindClusters* function with default Louvain algorithm. These clusters were manually aggregated and classified as T-cell subsets based on known markers. CD8 and CD4 T-cell classifications were based on both gene and protein expression of CD4, CD8α, and CD8β.

For subset analysis, the corresponding subsets were extracted from the master Seurat object using the *subset* function. The above detailed preprocessing steps were repeated to generate the corresponding UMAP and subset annotations.

Gene expression visualization

Gene expression was visualized in three ways: violin plots, heatmaps, and density plots. Violin plots were made based on normalized expression. Heatmaps were made based on average scaled expression, both using Seurat internal functions. Density plots were constructed using the Nebulosa package (version 1.6.0) to enhance visibility and mitigate sparsity of gene expression on UMAP. This is necessary for datasets with large number of cells (e.g. our $CD8^+$ CAR-T dataset has ~38k cells).

Differential gene expression (DEG) analysis on single-cell RNA-seq data

DEG analyses were by default performed using the *FindMarkers* function in Seurat package, with default parameters and the appropriate 'ident.1" and "ident.2" set as contrast. Unless otherwise stated, the results were filtered with p_val_adj <0.05 and abs(avg_log2FC) > 0.25. Moreover, we also performed additional DEG analyses through a pseudo-bulk approach to better control for patient-specific effects, using the LibraDEG package (version 1.0.0)[65] with default parameters (edgeR with LRT method). This was mainly performed when extracting timepoint-specific genes. Areas where this pseudo-bulk method is used are clearly stated in the figure legend.

Timepoint-specific gene signature validation

To validate the timepoint-specific molecular signatures shared across patients and against external data, we adopted two independent and complementary approaches: (1) correlation of timepoint-specific gene expression, (2) label transfer from our data to external data.

For the correlation approach, we first conducted pseudo-bulk DEG analyses of T_{exp} vs T_{per} across all patients and kept all the statistically significant genes (padj <0.05) as timepoint-specific genes. Note that we did not filter by log fold-change to include even weak timepoint-specific signatures. Essentially, the goal here is to remove all non-timepoint-specific genes that may confound correlation analysis. The normalized gene expressions of these timepoint-specific genes were extracted from both our data and the external data. Following that, average expression was calculated for each sample (patient by timepoint). Correlations were then calculated pairwise for all samples.

For the label transfer approach, we adapted the Seurat standard data integration and label transfer workflow with default parameters. This is a complementary approach where, rather than at patient-level expression, individual cells in the external data and our data could be compared and similar timepoint-labels could be assigned.

GSEA and pathway enrichment analysis

Gene Set Enrichment Analysis (GSEA) and pathway enrichment analysis were carried out using the clusterProfiler (version 4.4.4)[66] package based on the msigdb database built in msigdbr package (version 7.5.1)[67].

Exhaustion signatures from reference datasets

Besides standard msigdb exhaustion-related pathways, we obtained T-cell subset-specific signatures from Wherry et al. (see Supplementary

Table 1 in their study)[52]. The reference study provides the most updated and comprehensive $CD8^+$ (exhausted) T cell subsets, in the standard LCMV/Cl13 mouse models where T_{ex} was first defined. To refine the signature, we converted the mouse genes to their human orthologous genes and filtered the list to retain only the top 500 (by descending avg_log2_FC) statistically significant (p_val_adj <0.05) genes for each subset.

Regulon analysis

To construct regulons in a specific cell subset, we first extracted the raw count matrix of that subset. Then, we supplied it as input for the pySCENIC package (version 0.10.4) and ran through the workflow as detailed in its documentation and publication[68,69]. More specifically, the base script was adapted from the "PBMC10K" example script on the pyScenic website[70]. In addition, the arboreto component was used to speed up analysis. Each resultant regulon is a gene list with a central transcription factor and all its putative target genes determined through the SCENIC algorithm, and each set of regulons is sample/subset-specific and represents a putative regulatory unit in that specific sample/subset.

Regulon or general gene set signature scoring

Individual cells were scored using the AUCell package (version 1.10.0)[68] for a particular gene set from the msigdb database or from a single-cell-derived regulon as follows. The normalized gene expression was first used as input into the *AUCell_buildRankings* function to score each cell for gene set enrichment and to build a ranking matrix. The signature score was then calculated as an AUC score using the *AUCell_calcAUC* function with all default parameters. In later revisions, Ucell package (version 2.0.1)[71] was used in some re-analyses, as it is computationally more efficient and generates similar results as the AUCell package.

Machine learning classification on regulon scores

To classify $CD8^+$ CAR T cells at T_{exp} and T_{per}, we first built a regulon set for each subset independently, assuming that regulatory networks for each timepoint may be different. Then, we merged all regulon sets into a master regulon set. We calculated the regulon scores using the master regulon set for all cells from the two subsets, resulting in a regulon score matrix. Each cell then served as an observation and each regulon as a feature for machine learning.

The machine learning classification models were built in the caret framework using the caret package (version 6.0–90)[72]. Briefly, we divided the input data into training (75%), validation (15%), and test sets (10%). We trained and optimized xgboost models[73] through grid hyperparameter search and with a 5-fold cross-validation until reaching a best accuracy of >85% (refer to figures for specific accuracies).

We interrogated the final models for feature importance evaluation using the Shapley Additive Explanation (SHAP) method[74] implemented in the SHAPforxgboost package (version 0.1.1)[75]. Average SHAPley values were used to rank the regulons. Top timepoint-determining regulons were visualized and further analyzed.

Single-cell TCR-seq data processing

The TCR-seq reads from each sample were aligned to the 10x curated GRCh38 vdj reference genome and quantified using the cellranger vdj (10x Genomics, version 6.0.0). The results were then aggregated using the cellranger aggr function, with the source patient (donor) and timepoint (origin) of each sample supplied in the metadata to guide the clonotype assignment. The resultant clonotype and filtered contig annotation data were used for downstream analyses.

Single-cell TCR-seq tracing and phenotype linking

Each unique clonotype is defined by the amino acid and nucleotide sequence of CDR3 regions for paired productive TCRα and TCRβ chains. TCR clonality overlap and tracing analyses were carried out using the immunarch package (version 0.9.0)[76]. Clones with the same TCR CDR3 sequences from the same patient at different timepoints were re-grouped and traced from infusion product to the post-infusion samples.

Phenotype-to-clonotype linking: To identify T_{exp} and T_{per} precursors, clonotypes among post-infusion T_{exp} and T_{per} cell populations were identified respectively and traced back to the infusion product cells. When linking the TCR clonotype to the corresponding cell phenotype, we keep only data with matching cell barcodes from both the TCR-seq and RNA-seq data.

Abundance tracing: Clonal abundance for each CAR T clone is calculated as the percentage of all CAR T cells occupied by a clone at a given timepoint. Each clone was assigned a phenotype at each timepoint based on the most frequently occurring phenotype. T_{exp} clones that were predominantly EM-exh had their abundances tracked at T_{per1}/T_{per2}. T_{per1}/T_{per2} clones that were predominantly TE had their abundances tracked at T_{exp}.

CAR transgene mapping

The axicabtagene ciloleucel CAR design is documented[77]. Its sequence was confirmed by Sanger sequencing of genomic DNA extracted from axicabtagene ciloleucel infusion products. The CAR sequence was then added to the GRCh38 FASTA and GTF files accordingly. A custom reference for cellranger was built from these annotation files using cellranger mkref (10x Genomics, version 7.0.0). The resultant custom reference was used for CAR transgene mapping through cellranger count.

Inclusion and ethics statement

Roles and responsibilities were agreed amongst collaborators in advance. Our findings are not expected to result in stigmatization, incrimination, or discrimination.

Reporting summary

Further information on research design is available in the Nature Portfolio Reporting Summary linked to this article.

Data availability

All single-cell RNA-seq, CITE-seq, and TCR-seq data have been deposited in the Gene Expression Omnibus (GEO) and are available with the accession code GSE207192. Source data are provided with this paper.

Code availability

For reproducibility, code used for our analysis and figure-making is available on Zenodo: https://doi.org/10.5281/zenodo.15116870.

References

1. Diffuse Large B-Cell Lymphoma - Cancer Stat Facts. https://seer.cancer.gov/statfacts/html/dlbcl.html
2. Liu, Y. & Barta, S. K. Diffuse large B-cell lymphoma: 2019 update on diagnosis, risk stratification, and treatment. *Am. J. Hematol.* **94**, 604–616 (2019).
3. Longo, D. L., Sehn, L. H. & Salles, G. Diffuse large B-cell lymphoma. https://doi-org.proxy.uchicago.edu/10.1056/NEJMra2027612, **384**, 842–858 (2021).
4. June, C. H., O'Connor, R. S., Kawalekar, O. U., Ghassemi, S. & Milone, M. C. CAR T cell immunotherapy for human cancer. *Science* **359**, 1361–1365 (2018).
5. Neelapu, S. S. et al. Axicabtagene ciloleucel CAR T-cell therapy in refractory large B-cell lymphoma. *N. Engl. J. Med.* **377**, 2531–2544 (2017).
6. Schuster, S. J. et al. Tisagenlecleucel in adult relapsed or refractory diffuse large B-cell lymphoma. *N. Engl. J. Med.* **380**, 45–56 (2019).

7. Abramson, J. S. et al. Pivotal safety and efficacy results from transcend NHL 001, a multicenter phase 1 study of lisocabtagene maraleucel (liso-cel) in relapsed/refractory (R/R) large B cell lymphomas. *Blood* **134**, 241–241 (2019).
8. Abramson, J. S. et al. Lisocabtagene maraleucel for patients with relapsed or refractory large B-cell lymphomas (TRANSCEND NHL 001): a multicentre seamless design study. *Lancet* **396**, 839–852 (2020).
9. Locke, F. L. et al. Long-term safety and activity of axicabtagene ciloleucel in refractory large B-cell lymphoma (ZUMA-1): a single-arm, multicentre, phase 1–2 trial. *Lancet Oncol.* **20**, 31–42 (2019).
10. Schubert, M. L. et al. Side-effect management of chimeric antigen receptor (CAR) T-cell therapy. *Ann. Oncol.* **32**, 34–48 (2021).
11. Milone, M. C. et al. Engineering-enhanced CAR T cells for improved cancer therapy. *Nat. Cancer 2021 28* **2**, 780–793 (2021).
12. Good, Z. et al. Post-infusion CAR TReg cells identify patients resistant to CD19-CAR therapy. *Nat. Med.* **28**, 1860–1871 (2022).
13. Gupta, A. & Gill, S. CAR-T cell persistence in the treatment of leukemia and lymphoma. https://doi-org.proxy.uchicago.edu/10.1080/10428194.2021.1913146, **62**, 2587–2599 (2021).
14. Kawalekar, O. U. et al. Distinct signaling of coreceptors regulates specific metabolism pathways and impacts memory development in CAR T cells. *Immunity* **44**, 380–390 (2016).
15. Salter, A. I. et al. Phosphoproteomic analysis of chimeric antigen receptor signaling reveals kinetic and quantitative differences that affect cell function. *Sci. Signal.* **11**, 1–18 (2018).
16. Fraietta, J. A. et al. Determinants of response and resistance to CD19 chimeric antigen receptor (CAR) T cell therapy of chronic lymphocytic leukemia. *Nat. Med.* **24**, 563–571 (2018).
17. Rossi, J. et al. Preinfusion polyfunctional anti-CD19 chimeric antigen receptor T cells are associated with clinical outcomes in NHL. *Blood* **132**, 804–814 (2018).
18. Deng, Q. et al. Characteristics of anti-CD19 CAR T cell infusion products associated with efficacy and toxicity in patients with large B cell lymphomas. *Nat. Med.* **26**, 1878–1887 (2020).
19. Melenhorst, J. J. et al. Decade-long leukaemia remissions with persistence of CD4+ CAR T cells. *Nature* **602**, 503–509 (2022).
20. Finney, O. C. et al. CD19 CAR T cell product and disease attributes predict leukemia remission durability. *J. Clin. Invest* **129**, 2123–2132 (2019).
21. Neelapu, S. S. CAR-T efficacy: is conditioning the key? *Blood* **133**, 1799–1800 (2019).
22. Turtle, C. J. et al. CD19 CAR–T cells of defined CD4+:CD8+ composition in adult B cell ALL patients. *J. Clin. Invest.* **126**, 2123–2138 (2016).
23. Fraietta, J. A. et al. Disruption of TET2 promotes the therapeutic efficacy of CD19-targeted T cells. *Nature* 1 https://doi.org/10.1038/s41586-018-0178-z (2018).
24. Michelozzi, I. M. et al. The enhanced functionality of low-affinity CD19 CAR T cells is associated with activation priming and polyfunctional cytokine phenotype. *Blood* **136**, 52–53 (2020).
25. Jackson, Z. et al. Sequential single cell transcriptional and protein marker profiling reveals TIGIT as a marker of CD19 CAR-T cell dysfunction in patients with non-Hodgkin's lymphoma. *Cancer Discov*. https://doi.org/10.1158/2159-8290.CD-21-1586/696778/SEQUENTIAL-SINGLE-CELL-TRANSCRIPTIONAL-AND-PROTEIN (2022).
26. Sheih, A. et al. Clonal kinetics and single-cell transcriptional profiling of CAR-T cells in patients undergoing CD19 CAR-T immunotherapy. *Nat. Commun.* **11**, 1–13 (2020).
27. Haradhvala, N. J. et al. Distinct cellular dynamics associated with response to CAR-T therapy for refractory B cell lymphoma. *Nat. Med.* **28**, 1848–1859 (2022).
28. Hu, Y. et al. Antigen multimers: Specific, sensitive, precise, and multifunctional high-avidity CAR-staining reagents. *Matter* **4**, 1–24 (2021).
29. Lesch, S. et al. T cells armed with C-X-C chemokine receptor type 6 enhance adoptive cell therapy for pancreatic tumours. *Nat. Biomed. Eng. 2021 511* **5**, 1246–1260 (2021).
30. Davis, A. M., Ramos, H. J., Davis, L. S. & Farrar, J. D. Cutting edge: A T-bet-independent role for IFN-α/β in regulating IL-2 secretion in human CD4 + central memory T cells. *J. Immunol.* **181**, 8204–8208 (2008).
31. Kim, H. J. et al. Stable inhibitory activity of regulatory T cells requires the transcription factor Helios. *Science (80-)* **350**, 334–339 (2015).
32. Lee, J. C. et al. In vivo inhibition of human CD19-targeted effector T cells by natural T regulatory cells in a xenotransplant murine model of B cell malignancy. *Cancer Res.* **71**, 2871–2881 (2011).
33. Ciucci, T. & Bosselut, R. Gimap and T cells: A matter of life or death. *Eur. J. Immunol.* **44**, 348–351 (2014).
34. Evrard, M. et al. Sphingosine 1-phosphate receptor 5 (S1PR5) regulates the peripheral retention of tissue-resident lymphocytes. *J. Exp. Med.* **219**, (2021).
35. Zhang, L. et al. Etanercept as a new therapeutic option for cytokine release syndrome following chimeric antigen receptor T cell therapy. *Exp. Hematol. Oncol.* **10**, 4–7 (2021).
36. Daniels, M. A., Luera, D. & Teixeiro, E. NFκB signaling in T cell memory. *Front. Immunol.* **14**, 1–12 (2023).
37. Park, S. L. & Mackay, L. K. Bhlhe40 keeps resident T cells too fit to quit. *Immunity* **51**, 418–420 (2019).
38. Lynn, R. C. et al. c-Jun overexpression in CAR T cells induces exhaustion resistance. *Nature* **576**, 293–300 (2019).
39. Stelekati, E. et al. Long-term persistence of exhausted CD8 T cells in chronic infection is regulated by MicroRNA-155. *Cell Rep.* **23**, 2142–2156 (2018).
40. Chen, Z. et al. In vivo CD8+ T cell CRISPR screening reveals control by Fli1 in infection and cancer. *Cell* **184**, 1262–1280.e22 (2021).
41. Zhou, M., Clayberger, C. & Krensky, A. M. Krüppel-like transcription factor 13 regulates T lymphocyte survival in vivo. *J. Immunol.* **178**, 5496–5504 (2007).
42. Xu, B. et al. The chromatin remodeler BPTF activates a stemness gene-expression program essential for the maintenance of adult hematopoietic stem cells. *Stem Cell Rep.* **10**, 675–683 (2018).
43. Wu, B. et al. BPTF is essential for T cell homeostasis and function. *J. Immunol.* **197**, 4325–4333 (2016).
44. Mamonkin, M., Puppi, M. & Lacorazza, H. D. Transcription factor ELF4 promotes development and function of memory CD8+ T cells in Listeria monocytogenes infection. *Eur. J. Immunol.* **44**, 715–727 (2014).
45. Jenne, C. N. et al. T-bet-dependent S1P5 expression in NK cells promotes egress from lymph nodes and bone marrow. *J. Exp. Med.* **206**, 2469–2481 (2009).
46. Walker, A. J. et al. Tumor antigen and receptor densities regulate efficacy of a chimeric antigen receptor targeting anaplastic lymphoma kinase. *Mol. Ther.* **25**, 2189–2201 (2017).
47. Rodriguez-Marquez, P. et al. CAR density influences antitumoral efficacy of BCMA CAR T cells and correlates with clinical outcome. *Sci. Adv.* **8** https://www.science.org (2022).
48. Wilson, T. L. et al. Common trajectories of highly effective CD19-specific CAR T cells identified by endogenous T cell receptor lineages. *Cancer Discov*. https://doi.org/10.1158/2159-8290.CD-21-1508/3166017/cd-21-1508.pdf (2022).
49. Giles, J. R. et al. Human epigenetic and transcriptional T cell differentiation atlas for identifying functional T cell-specific enhancers. *Immunity* **55**, 557–574.e7 (2022).
50. Chen, P. H. et al. Activation of CAR and non-CAR T cells within the tumor microenvironment following CAR T cell therapy. *JCI Insight* **5**, (2020).

51. Blank, C. U. et al. Defining 'T cell exhaustion. *Nat. Rev. Immunol.* **19**, 665–674 (2019).
52. Giles, J. R. et al. Shared and distinct biological circuits in effector, memory and exhausted CD8+ T cells revealed by temporal single-cell transcriptomics and epigenetics. *Nat. Immunol.* **23**, 1600–1613 (2022).
53. Shah, N. N. et al. Clonal expansion of CAR T cells harboring lentivector integration in the CBL gene following anti-CD22 CAR T-cell therapy. *Blood Adv.* **3**, 2317–2322 (2019).
54. Goldberg, L. et al. Single-cell analysis by mass cytometry reveals CD19 CAR T cell spatiotemporal plasticity in patients. *Oncoimmunology* **11**, (2022).
55. Li, X. et al. Single-cell transcriptomic analysis reveals BCMA CAR-T cell dynamics in a patient with refractory primary plasma cell leukemia. *Mol. Ther.* **29**, 645–657 (2021).
56. Chavez, J. C., Bachmeier, C. & Kharfan-Dabaja, M. A. CAR T-cell therapy for B-cell lymphomas: Clinical trial results of available products. *Ther. Adv. Hematol.* **10**, 2040620719841581 (2019).
57. Chen, G. M. et al. Integrative bulk and single-cell profiling of premanufacture T-cell populations reveals factors mediating long-term persistence of CAR T-cell therapy. *Cancer Discov.* 1677.2020 https://doi.org/10.1158/2159-8290.cd-20-1677 (2021).
58. Zhao, Z. et al. Structural design of engineered costimulation determines tumor rejection kinetics and persistence of CAR T cells. *Cancer Cell* **28**, 415–428 (2015).
59. Maude, S. L. et al. Tisagenlecleucel in children and young adults with B-cell lymphoblastic leukemia. *N. Engl. J. Med.* **378**, 439–448 (2018).
60. Mackensen, A. et al. Anti-CD19 CAR T cell therapy for refractory systemic lupus erythematosus. *Nat. Med.* **28**, 2124–2132 (2022).
61. Stoeckius, M. et al. Simultaneous epitope and transcriptome measurement in single cells. *Nat. Methods 2017 149* **14**, 865–868 (2017).
62. What is Cell Ranger? -Software -Single Cell Gene Expression -Official 10x Genomics Support. https://support.10xgenomics.com/single-cell-gene-expression/software/pipelines/latest/what-is-cell-ranger.
63. Hao, Y. et al. Integrated analysis of multimodal single-cell data. *Cell* **184**, 3573–3587.e29 (2021).
64. Korsunsky, I. et al. Fast, sensitive and accurate integration of single-cell data with Harmony. *Nat. Methods* **16**, 1289–1296 (2019).
65. Squair, J. W. et al. Confronting false discoveries in single-cell differential expression. *Nat. Commun.* **12**, (2021).
66. Wu, T. et al. clusterProfiler 4.0: A universal enrichment tool for interpreting omics data. *Innov.* **2**, (2021).
67. Subramanian, A. et al. Gene set enrichment analysis: A knowledge-based approach for interpreting genome-wide expression profiles. *Proc. Natl. Acad. Sci. USA* **102**, 15545–15550 (2005).
68. Aibar, S. et al. SCENIC: Single-cell regulatory network inference and clustering. *Nat. Methods* **14**, 1083–1086 (2017).
69. Van de Sande, B. et al. A scalable SCENIC workflow for single-cell gene regulatory network analysis. *Nat. Protoc. 2020 157* **15**, 2247–2276 (2020).
70. PBMC10k_downstream-analysis. http://htmlpreview.github.io/?. https://github.com/aertslab/SCENICprotocol/blob/master/notebooks/PBMC10k_downstream-analysis.html.
71. Andreatta, M. & Carmona, S. J. UCell: Robust and scalable single-cell gene signature scoring. *Comput. Struct. Biotechnol. J.* **19**, 3796–3798 (2021).
72. Kuhn, M. Building Predictive Models in R Using the caret Package. *J. Stat. Softw.* **28**, 1–26 (2008).
73. Tianqi, C. & Guestrin, C. XGBoost: A scalable tree boosting system. *KDD* (2016).
74. Lundberg, S. M. & Lee, S. I. A unified approach to interpreting model predictions. *Adv. Neural Inf. Process. Syst.* **2017**, 4766–4775 (2017).
75. Liu, Y. & Just, A. SHAPforxgboost: SHAP Plots for 'XGBoost'. (2020).
76. ImmunoMind Team. immunarch: An R package for painless bioinformatics analysis of T-cell and B-cell immune repertoires. https://doi.org/10.5281/zenodo.3367200 (2019).
77. Kochenderfer, J. N. et al. Construction and preclinical evaluation of an anti-CD19 chimeric antigen receptor. *J. Immunother.* **32**, 689–702 (2009).

Acknowledgements

We thank Phi Beta Psi, the Ullman Fund in Cancer Immunology, the Hoogland Lymphoma Research Pilot Projects, Chicago Immunoengineering Innovation Center, American Cancer Society Scholar Award (SG-22-136-01-1BCD) and NIH New Innovator award (1DP2AI144245) for financial support (to J.H.). Y.H. was supported by the University of Chicago MSTP Training Grant (T32GM007281). T.P. was supported by the University of Chicago CSTR training grant (T32HL007381). N.A. was supported by the University of Chicago MTCR training grant (T32CA009594). This project was supported by the National Center for Advancing Translational Sciences of the National Institutes of Health through Grant Number 5UL1TR002389-02 that funds the Institute for Translational Medicine. We thank the UChicago Human Immunologic Monitoring Facility for patient biospecimen cryopreservation, as well as the Pritzker School of Molecular Engineering Single-Cell Immunophenotyping Core and UChicago Genomics Facility for instrumentation to generate single-cell sequencing data. This work was completed in part with resources provided by the University of Chicago's Research Computing Center. The authors thank Dr. Karen M. Watters for scientific editing of the manuscript.

Author contributions

Y.H., G.C., J.P.K., and J.H. conceived and designed all experiments. J.H. supervised the project. T.A., P.A.R., and M.R.B. coordinated patient biospecimens for these studies. G.C. and T.P. performed all single-cell and machine-learning analyses. Y.H. organized execution of all experiments. Y.H. and E.T. sorted CAR T cells and generated single-cell data. G.C. and Y.H. jointly interpreted data. N.A. and Y.H. designed cartoons. E.T. performed flow cytometry validation. Y.H. and G.C. prepared the manuscript. J.H. and J.P.K. edited the manuscript. All authors reviewed the manuscript.

Competing interests

P.A.R. reports Research Support/Funding: BMS, Kite Pharma, Inc./Gilead, MorphoSys, Calibr, Tessa Therapeutics, Fate Therapeutics, Xencor, and Novartis Pharmaceuticals Corporation. Speaker's Bureau: Kite Pharma, Inc./Gilead; Consultancy on advisory boards: AbbVie, Novartis Pharmaceuticals Corporation, BMS, Janssen, BeiGene, Karyopharm Therapeutics Inc., Takeda Pharmaceutical Company, Kite Pharma, Inc./Gilead, Sana Biotechnology, Nektar Therapeutics, Nurix Therapeutics, Intellia Therapeutics, and Bayer. Honoraria: Novartis Pharmaceuticals Corporation. M.R.B. reports Membership on an Advisory Board or Consultancy for Kite/Gilead, Novartis, CRISPR Therapeutics, Autolus Therapeutics, BMS, Incyte, Sana Biotechnology, Iovance Biotherapeutics. He has served on a Speakers Bureau for BMS, Kite/Gilead, Agios, and Incyte. J.P.K. receives research support from Merck, Verastem, and iTeos; has served on a speaker's bureau for Kite/Gilead; and has served on advisory boards for Verastem, Seattle Genetics, MorphoSys, and Karyopharm. The remaining authors declare no competing interests.

Additional information

Supplementary information The online version contains supplementary material available at https://doi.org/10.1038/s41467-025-59298-w.

Correspondence and requests for materials should be addressed to Jun Huang.

Peer review information *Nature Communications* thanks the anonymous reviewer(s) for their contribution to the peer review of this work. A peer review file is available.